THESIS FOR THE DEGREE OF DOCTOR OF PHILOSOPHY

ADVANCES IN HOLOGRAPHIC OPTICAL TRAPPING

Martin Persson

Department of Physics
University of Gothenburg

Gothenburg, Sweden 2013

UNIVERSITY OF GOTHENBURG

Cover: A phase hologram, generated with a modified Gerchberg-Saxton algorithm, producing an array of 5×5 spots in its Fourier plane.

Advances in Holographic Optical Trapping

Martin Persson

Department of Physics, University of Gothenburg

Abstract

Holographic optical trapping (HOT) is a technique for non-invasive dynamic manipulation of multiple microscopic objects, which has been used for many applications in the life sciences during the past decade. The technique uses holographic beam steering with a spatial light modulator (SLM) to direct light to the desired positions of optical traps. In many cases, the control of the optical intensity of the traps is impaired by imperfections in the SLM. This has limited the use of HOT for applications sensitive to variations in the trap intensities, such as optical force measurement (OFM). Also, the algorithms for optimization of holograms used in HOT are computationally demanding, and real-time manipulation with optimized holograms has not been possible.

In this thesis, four different methods for improving the accuracy of holographic beam steering are presented, along with a novel application for the combination of HOT and position measurement. The control of trap intensities is improved by compensating for crosstalk between pixels, and for spatial variations of the phase response of the SLM; and by dumping a controlled amount of light to specified regions away from the traps. Variations in trap intensities occurring when updating the SLM with new holograms are suppressed by enforcing a stronger correlation between consecutive holograms. The methods consist of modifications of the algorithm used for hologram generation, or alternative methods for post-processing of generated holograms. Applications with high stability requirements, such as OFM with HOT, will benefit from the presented improvements. A method for reducing computation time for hologram optimization is also presented, allowing the accuracy improvements to be used also for time critical applications.

Further, it is shown that position measurement of nanowires, held by multiple optical traps, can be used to probe the orientational structure and defects in liquid crystal materials.

This thesis is based on the work contained in the following scientific papers.

I **Minimizing intensity fluctuations in dynamic holographic optical tweezers by restricted phase change**
Martin Persson, David Engström, Anders Frank, Jan Backsten, Jörgen Bengtsson, and Mattias Goksör
Optics Express, **18**(11), 11250–11263, (2010).

II **Three-dimensional imaging of liquid crystal structures and defects by means of holographic manipulation of colloidal nanowires with faceted sidewalls**
David Engström, Rahul P. Trivedi, **Martin Persson**, Mattias Goksör, Kris A. Bertness and Ivan I. Smalyukh
Soft Matter, **7**, 6304–6312, (2011).

III **Real-time generation of fully optimized holograms for optical trapping applications**
Martin Persson, David Engström and Mattias Goksör
Proceedings of SPIE, **8097**, 80971H, (2011).

IV **Unconventional structure-assisted optical manipulation of high-index nanowires in liquid crystals**
David Engström, Michael C.M. Varney, **Martin Persson**, Rahul P. Trivedi, Kris A. Bertness, Mattias Goksör, and Ivan I. Smalyukh
Journal, **20**(7), 7741–7748, (2012).

V **An algorithm for improved control of trap intensities in holographic optical tweezers**
Martin Persson, David Engström, Mattias Goksör
Proceedings of SPIE, **8458**, 84582W-1, (2012).

VI **Reducing the effect of pixel crosstalk in phase only spatial light modulators**
Martin Persson, David Engström, and Mattias Goksör
Optics Express, **20**(20), 22334–22343, (2013).

My contributions to the appended papers:

Paper I. I developed and implemented the new algorithm, designed the experimental setup, planned and conducted the experiments and wrote the paper.

Paper II. I participated in planning and conducting most of the experiments. I assisted in writing the paper.

Paper III. I developed two out of the four described methods, implemented all methods in software for fast hologram generation, planed and conducted the measurements and wrote the paper.

Paper IV. I participated in planning and conducting most of the experiments. I assisted in writing the paper.

Paper V. I developed and implemented the algorithm, designed the experimental setup, conducted the measurements and wrote the paper.

Paper VI. I developed and implemented the algorithm, conducted the measurements and wrote the paper.

Paper VII. I participated in planning and conducting the experiments. I assisted in writing the paper.

Contents

Chapter 1

Introduction

1.1 Optical Trapping

The history of optical trapping dates back to 1970, when Arthur Ashkin showed how micrometer sized latex spheres could be trapped in the region of highest intensity of two counter propagating laser beams [1]. Ashkin and coworkers at Bell Laboratories investigated optical levitation and dual beam trapping of dielectric objects and atoms throughout the 1970:s and early 80:s, gaining relatively little attention. In 1978, Ashkin suggested the use of a single highly focused Gaussian beam for atom trapping [2,3], the technique now known as Optical Tweezers (OT). A true milestone in optical trapping was reached some eight years later, when Ashkin, along with Steven Chu experimentally demonstrated that optical tweezers could be used for stable trapping of both micron sized dielectric particles and atoms [4, 5]. While Chu pursued refining atom trapping and cooling, for which he was awarded the Nobel Prize in physics in 1997, Ashkin continued developing applications for the optical tweezers in cell biology [6]. Optical trapping has since found many applications in cell and molecular biology and in soft matter physics.

Soon after OT was invented it was found that optically trapped objects could be used as a force transducers to measure minute external forces. This is possible since the attractive optical force on a trapped object is proportional to its distance from its equilibrium position. The technique, which requires the combination of optical tweezers with a position measurement system, is known as Optical Force Measurement (OFM). It has since then been refined to resolve forces in the piconewton range and even smaller and now provides unrivaled accuracy for non invasive force measurements on living specimens [7, 8].

1.2 Holographic Optical Tweezers

In 1998, Dufresne and Grier [9] demonstrated how multiple optical traps could be generated by introducing a diffractive optical element (DOE) in the beam path of an OT setup. The system was called "the hexadeca tweezer" and may be seen as the starting point for the development of what is now better known as Holographic Optical Tweezers (HOT). In 1999, Reicherter *et al.* [10] showed that by replacing the DOE with a phase modulating *spatial light modulator* (SLM) connected to a computer, the wave front entering the microscope objective could be dynamically altered to change the resulting trap configuration. The technique soon became widely used due to its increased flexibility and user friendliness; optical traps could now be created on demand and repositioned in real time by the user. HOT is now the dominating technique for parallel optical trapping and with ever increasing performance and availability of spatial light modulators, it is likely to keep finding new applications in a wide range of fields.

OFM and HOT are two techniques that both have been widely used in the life sciences during the past decade, and the combination of OFM and HOT has become increasingly popular [11–15]. It allows for parallel investigation on multiple objects for increased throughput or simultaneous measurements on multiple sites on a single object, e.g., to reveal spatial variations in parameters such as thickness, density and viscosity of the cell coat. Combining the two techniques, however, has proved difficult and the accuracy of force measurements with HOT systems has so far been inferior to the accuracy obtained with single tweezers. The main limitation has been in controlling the intensities of individual traps in HOT systems. Methods for optimizing holograms for precise control of the output field have since long been available but have, due to extensive computation time, been impractical for real-time applications. The use of non-ideal SLMs has also prevented the intensities of the traps to reach predicted values.

1.3 Structure of this Thesis

The work presented in this thesis has aimed at enabling the use of HOT for new applications. Much work has been devoted to improve the beam steering accuracy of HOT systems, with the specific goal to enable OFM capabilities comparable with single trap OFM systems. Several methods for increasing control over trap intensities are presented, and it is demonstrated how highly optimized holograms can be used also for time critical real-time applications. A novel application is also presented, where a HOT system is used to characterize liquid crystal materials by an unconventional optical manipulation method.

After an introduction to optical tweezers and holographic optical trapping in

chapter 2, the algorithms used for hologram generation are presented in chapter 3, including a modified algorithm improving the control of the trap intensities. A brief description of nematic liquid crystal materials is given in chapter 4, and the liquid crystal based SLMs used in this work are described in chapter 5. Several methods for improving their performance by correcting for inherent errors and limitations are also presented in this chapter. A review of methods for optical force measurements is given in chapter 6 and our software for fast hologram generation is described in chapter 7. Chapter 8 describes a technique for characterizing liquid crystal materials using optically trapped semiconductor nanowires, and is followed by a conclusion in chapter 9

Chapter 2

Optical Trapping

2.1 Optical Forces

Light carries not only energy but also momentum, and can hence exert forces on objects through momentum transfer. This was suggested by Johannes Kepler in the 17:th century, theoretically substantiated by James Clerk Maxwell in the late 19:th century and experimentally demonstrated by Pyotr Lebedev around 1900 [16]. It was not until the invention of the laser that sufficient light intensities could be obtained for the forces to be substantial, and few practical experiments were conducted until Ashkin started experimenting with optical trapping in the 1970:s. In this section, a qualitative description of the forces involved in optical trapping will be given. For a more comprehensive understanding of the underlying theory and methods for numerical calculation of optical forces, please refer to references [4, 17, 18].

Optical forces acting on an object can be understood by observing how the direction and intensity of light, and thereby its momentum, is changed by the object. Following the law of conservation of momentum, any change in momentum caused by the object must be accompanied by an equal, opposite signed change in the momentum of the object itself. Taking a single photon encountering a perfectly absorbing object as an elemental example (1a and 1b in figure 2.1), it is easy to realize that all momentum carried by the photon, $\boldsymbol{p}_0$, must be transferred to the object upon impact (1b). If the photon instead is reflected along the normal of a perfectly reflective surface (2a), the reversal of the direction of the pulse must be accompanied by a transfer of momentum to the surface with twice the magnitude, and same direction, as the momentum originally carried by the photon (2b). In a third example, a prism is considered (3a). The prism changes the direction of the photon (3b), which hence obtains a momentum in the transverse direction, and a decreased momentum in the axial direction. The prism must therefore have gained a momentum whose magnitude, αp_0, and direction are dictated by Snell's law and the laws of energy
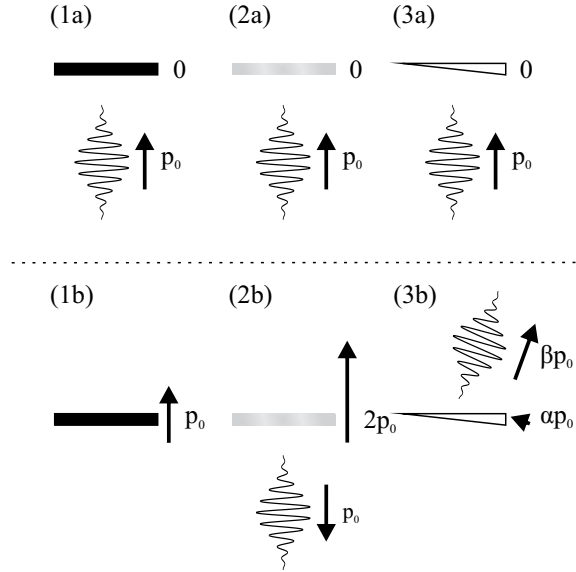
(1a)   (2a)   (3a)

Figure 2.1: Illustration of the momentum transfer between a single photon and materials with different optical properties. The momenta are shown to the right of the materials and the photon before (a) and after (b) impact. In (1a) and (1b) the material is perfectly absorbing and therefore gains the total momentum of the photon. In (2a) and (2b), the material is perfectly reflective and gains a momentum with double the magnitude and same direction as the photon before impact. In (3a) and (3b), the material changes the direction of the photon in the lateral direction and gains a momentum in a direction opposite to the change. Note that a light pulse of finite length does not have a well defined momentum but is here used as an illustration of the single photon.

and momentum conservation.

If instead a continuous beam of light is being refracted, reflected or absorbed by an object, the optical force exerted on the object is given by the change of the total *momentum flux*, $\boldsymbol{\rho}$, of the beam, $\boldsymbol{F} = \Delta\boldsymbol{\rho}$. Figure 2.2 illustrates a spherical transparent bead, located in different positions around the beam waist of a focused laser beam. The bead changes the direction and magnitude of the momentum flux of the beam and thereby experiences an optical force, $\boldsymbol{F}$. The bead here acts like a positive lens that, when displaced in the lateral x-direction from the center (a), changes the direction of the beam, and when displaced in the axial z-direction (b and c), changes the focusing of the beam and thereby the magnitude of its net momentum flux. Note that the bead increases the convergence of the beam when positioned before the beam waist (b), decreasing the net momentum of the beam; and decreases the divergence when positioned after the waist (c), increasing the net momentum of the beam. The resulting optical force, $\boldsymbol{F}$, has a direction opposite to the difference of the
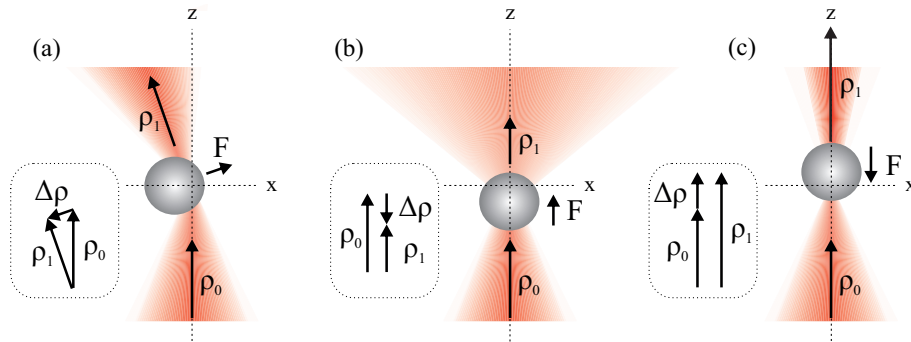
Figure 2.2: Illustration of the momentum transfer between a focused Gaussian light beam and a spherical particle in the vicinity of the beam waist. In each situation (a, b and c) the displacement of the bead from the center causes a change in momentum flux of the beam in the same direction as the displacement. In accordance with Newton's third law of motion, the bead must then experience a reaction force, restoring the bead to the center of the beam. Reflections in the surface of the bead are here neglected.

momentum flux vector of the beam before and after passage through the bead, $\Delta\boldsymbol{\rho} = \boldsymbol{\rho}_1 - \boldsymbol{\rho}_0$. The optical force therefore always points in the direction opposite from the displacement. It is therefore called the *restoring force* and may lead to stable trapping of the bead near the center of the beam waist.

In figure 2.2 and its description, an important factor has been neglected. When a beam of light encounters an interface between two dielectric media with different refractive indices, the beam is partly reflected. The reflection always gives a momentum transfer with a positive axial component, and will push the interface in the direction of the beam. As a result, a bead trapped in a focused laser beam will find its equilibrium position slightly after the beam waist. For stable trapping in three dimensions, the axial component of the restoring force must be larger than the axial component of the force resulting from reflections, the *scattering force*. This can only be obtained if the trapping beam is strongly focused. Particles with high refractive index relative to the surrounding medium, and thereby strong reflections in its surfaces, may not be trappable even in a highly focused beam. Such a particle may, however, be optically trapped in two dimensions, e.g., when pushed towards a surface.

2.2   Single Trap Setup

An optical tweezers setup is usually built around an inverted optical microscope with a high numerical aperture (NA) objective. By using the microscope objective both for imaging of the sample and focusing of the laser beam, the trap can be conveniently positioned in the center of the field of view of the microscope.
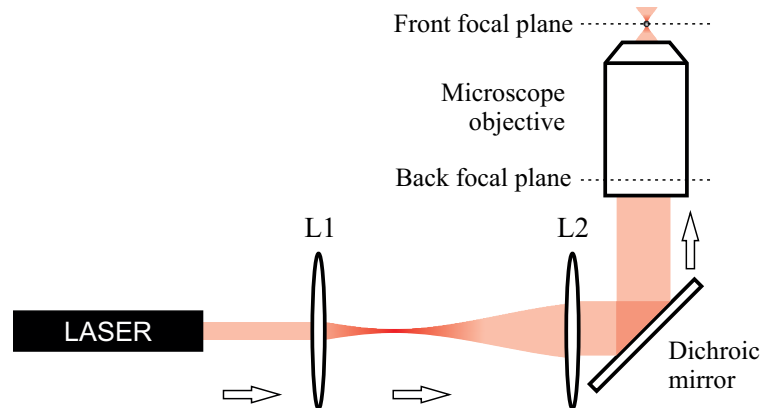
Figure 2.3: Sketch of an optical tweezers setup. The trapping beam is expanded by lenses L1 and L2 and reflected into the light path of the microscope by a dichroic mirror designed to transmit the illumination light of the microscope. The beam enters the objective through its back aperture and focuses to a diffraction limited spot in the image plane (the front focal plane of the objective).

For biological applications, the wavelength of the trapping laser is preferably in the near infrared spectrum, rather than the visible, to reduce photo damage of the sample [19, 20]. Figure 2.3 shows a sketch of a typical optical tweezers setup. The beam is reflected into the light path of the microscope by a dichroic mirror designed for reflectance of the trapping beam and high transmission of the visible spectrum, and positioned below the rear aperture of the objective. This arrangement requires a minimum of modifications of the microscope, and allows for the combination with most advanced fluorescence imaging techniques. Lenses L1 and L2 constitute an afocal telescope, expanding the beam to match or slightly overfill the exit pupil of the microscope objective. A slight overfilling has been shown to result in optimal three dimensional trapping performance [21]. The trap can be displaced in the lateral plane by changing the angle of incidence of the laser beam in the *back focal plane* (BFP) of the objective. To maintain the intensity and symmetry of the trap, this should be done without changing the position of the beam at the exit pupil of the objective, usually coinciding with its BFP [22]. A common method for achieving this is to introduce a gimbal mounted mirror in a plane conjugate to the BFP, having its center of rotation on the optical axis of the system.

2.3 Multiple Trap Setups

Multiple traps can be created and individually controlled using lasers with different wavelengths brought into a common path using dichroic mirrors, or by

separating orthogonal polarization directions of a beam and recombining them after passing through beam steering optics [22]. By rapidly scanning the angle of a mirror in the BFP, multiple objects can be trapped using a single beam [23]. This is called time-multiplexing and may also be achieved with an acousto-optical deflector placed so that the beam pivots around the center point of the BFP. The repetition rate of the scanning must be much faster than the diffusion time required for the object to escape the trap, which usually is several kHz. A large number of objects can be trapped simultaneously with this technique but traps are restricted to a single plane.

Using diffractive optics, light from a single laser beam can be distributed into arbitrary trap configurations, also along the optical axis of the system. Similarly to the use of beam steering mirrors, the diffractive optical element is normally positioned in a plane conjugate to the BFP to maintain a Gaussian intensity profile of the diffraction spots.

2.4   Holography

With an SLM, the trap arrangement can be changed dynamically. SLMs used for optical trapping can be thought of as reflective dynamic DOEs, whose phase modulations are reconfigurable from a computer. Optical traps can be moved in the sample volume of the microscope by calculating series of phase patterns that, when transferred to the SLM in sequence, displace the traps in small steps. When the SLM displays a phase pattern giving a desired intensity distribution in the trapping plane, it has the function of a hologram. The technique is thus called holographic optical trapping. A typical HOT-setup is shown in figure 2.4. The SLM is imaged onto the BFP of the objective using lenses (L1 and L2 in figure 2.4), whose focal lengths are chosen so that the image of the active area of the SLM matches the size of the exit pupil of the microscope objective. The beam expander is in turn designed so that the trapping beam slightly overfills the active area of the SLM to obtain optimal three dimensional trapping as described in section 2.2. In practice, the HOT setup is merely a slight modification of the single trap setup, such systems can easily be converted for HOT capabilities. In the following chapters, methods for designing holograms that give optimal intensity in the trap positions will be described.
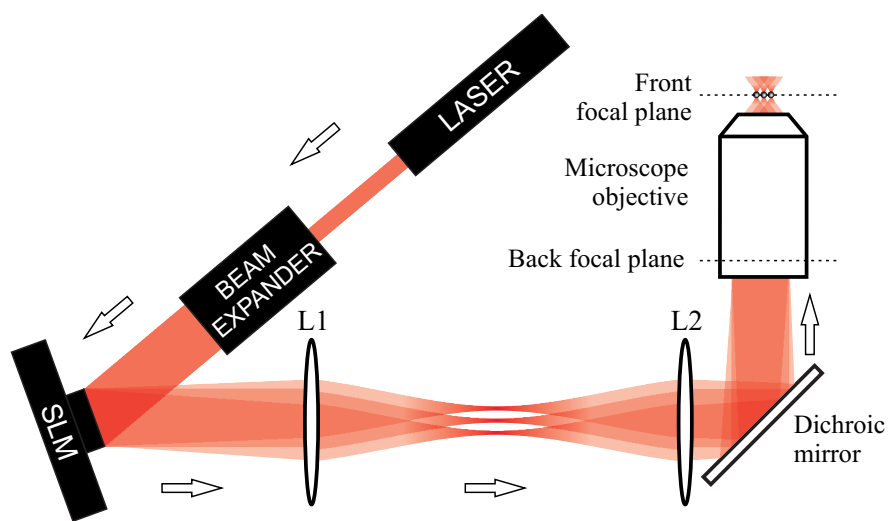
Figure 2.4: Sketch of a holographic optical trapping setup. The laser beam passes through a beam expander to match, and slightly overfill, the active area of the SLM. After reflection on the SLM surface, the lenses L1 and L2 image the SLM onto the back focal plane of the microscope objective. The Fourier plane of the SLM hence coincides with the image plane of the microscope.

Chapter 3

Holographic Beam Steering

To control optical traps holographically, a method for correctly addressing the SLM given the desired trap positions and intensities is required. The problem can be broken down into two main tasks; the first task is to find an optical field at the plane of the SLM, resulting in the desired intensities after the field has propagated to the trap positions. This field will here be referred to as the *ideal hologram*. When calculating the ideal hologram, it is assumed that its phase can take any value in a range of 0–2π in all pixels, while the amplitude is restricted to the amplitude distribution of incident light, since SLMs used in HOT setups typically are phase modulating only. The propagation is mathematically described by scalar diffraction theory, and relevant expressions will be derived in section 3.1. When only phase modulation is possible, the first task usually lack an exact solution and is thus an optimization problem. Algorithms for optimizing the ideal hologram will be presented in section 3.2, including an improved algorithm which is also presented in Paper V.

The second task is to address the SLM pixels so that the physical field created by the SLM resembles the ideal hologram as closely as possible. This requires careful characterization of the SLM and efficient methods for compensating for its limitations and non-ideal behaviour. Both characterization and compensation methods are presented in Paper I, VI and VII and will be discussed in further detail in section 5.2.

3.1   Scalar Diffraction

This section will provide a brief review of the mathematical framework used for numerical propagation of the light field within the paraxial limit, which is extensively used in the hologram generating algorithms described in section 3.2. The material in this section is based on work by J. W Goodman [24] with the mathematical expressions adapted for our optical system.

3.1.1   The Rayleigh-Sommerfelt Diffraction Integral

In the early 19:th century, the so called *Huygens-Fresnel principle* was presented by Augustine Jean Fresnel, who combined Huygens' intuitive description of wave propagation with the principle of superposition to obtain a mathematical expression for the diffraction of light passing through an aperture in an opaque screen. The Huygens-Fresnel principle states that the field at some distance from a diffracting aperture can be calculated as the superposition of secondary spherical waves emerging from the aperture. An *inclination factor* was introduced by Fresnel to obtain agreement with experimental data. Gustav Kirchhoff later showed that a similar expression could be derived by applying Green's theorem to the Helmholtz equation for a monochromatic wave and assuming appropriate boundary conditions on the field at the screen. The expression presented by Fresnel, including the inclination factor, was thereby given a firm mathematical substantiation with its foundation in Maxwell's equations. In his derivations, Kirchhoff assumed that both the field and its derivative at the screen outside the aperture equaled zero. These conditions were found to be mutually inconsistent by Arnold Sommerfeld, as they would require the field in the entire half space after the screen to equal zero. Sommerfeld used a different implementation of the Green's theorem and applied the boundary condition only to the field itself, avoiding the inconsistency, and arrived at the expression known as the *Rayleigh-Sommerfeld* (RS) diffraction integral. With the RS integral, the optical field in a spatial position (u, v, z), with $z > 0$, is given by

$$U(u, v, z) = \frac{1}{i\lambda} \iint_{\Sigma} U(x, y, 0) e^{ikr} \frac{cos(\theta)}{r} dx dy, \qquad (3.1)$$

where Σ is the aperture surface, positioned at $z = 0$, $U(x, y, 0)$ is the field within the aperture, r is the length of a vector connecting the evaluation points and points on the aperture, given by $r = \sqrt{z^2 + (x - u)^2 + (y - v)^2}$, and θ is its angle to the surface normal.

3.1.2   The Fresnel Diffraction Integral

A common simplification of the RS diffraction formula is given by the *paraxial approximation*, valid for small θ. Using the binomial expansion of $\sqrt{1 + b}$ for $b = \frac{(x-u)^2 + (y-v)^2}{z^2}$, r can be rewritten as

$$r \approx z + \frac{1}{2} \frac{(x - u)^2 + (y - v)^2}{z}. \qquad (3.2)$$

Using this expression for the rapidly oscillating phase factor e^{ikr} in equation 3.1, and only the first order term for other factors, so that $cos\theta / r = z/r^2 \approx 1/z$,

the *Fresnel diffraction integral* is obtained,

$$U(u, v, z) = \frac{e^{\mathrm{i}kz}}{\mathrm{i}\lambda z} \iint_{-\infty}^{\infty} U(x, y, 0) e^{\mathrm{i}\frac{k}{2z}(x-u)^2 + (y-v)^2} du dv, \tag{3.3}$$

here written in convolution form.

3.1.3 Propagation to Target Position

To calculate the field in the desired position of an optical trap, it would seem that the field in the plane of the SLM must be numerically propagated through the entire optical system. Recalling the geometry of the typical HOT system described in figure 3.1, this task may seem rather complex due to the multitude of optical components between the SLM and the trap positions. A much simplified situation is obtained by considering the second lens, L2, and the microscope objective as a perfect imaging unit, translating the trap arrangement to a region between the lenses L1 and L2 without aberrations. The problem then reduces to propagation through free space from the plane of the SLM to the lens L1, propagation through the lens, and through free space to the positions of the traps as imaged through L2 and the objective, from here on referred to as the *target positions*.
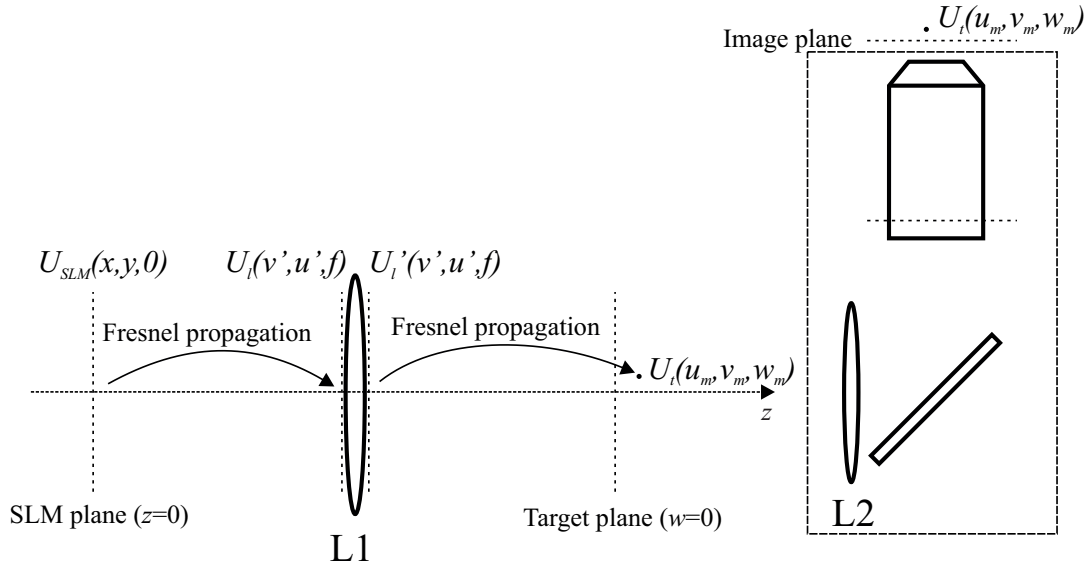

Figure 3.1: Diagram describing the numerical propagation to the a target position. The optical components inside the dashed box are assumed to constitute a perfect imaging system, so that the field in a point near the image plane of the microscope is given exactly by its image near the target plane.

The lens L1 is positioned at its focal distance, f, from the SLM. The field at its front surface is thus obtained by applying the Fresnel diffraction integral to the field at the plane of the SLM, $U_{SLM}(x, y) = U{x, y, 0}$, which yields

$$U_l(u', v', f) = \frac{e^{\mathrm{i}kf}}{\mathrm{i}\lambda f} \iint_{-\infty}^{\infty} U_{SLM}(x, y) e^{\mathrm{i}\frac{k}{2f}((x-u')^2 + (y-y')^2))} dx dy, \qquad (3.4)$$

where (u', v') are the lateral coordinates in the plane of this lens. With the thin lens approximation, the field at the rear surface of the lens, $U_l'(u', v', f)$, is given by multiplication with $e^{-\mathrm{i}\frac{k}{2f}(u'^2 + v'^2)}$, exactly canceling the quadratic phase term in the intermediate coordiates, (u', v') in equation 3.4. Applying the diffraction integral to $U_l'(u', v', f)$ for propagation to a (u, v) plane at a distance $f + w$ from the lens L1 yields an expression for the entire propagation. Evaluating the integral over the intermediate coordinates then gives

$$U_t(u, v, w) = \frac{1}{\mathrm{i}\lambda f} e^{\mathrm{i}\frac{2\pi(2f+w)}{\lambda}} \iint_{-\infty}^{\infty} U_{SLM}(x, y) e^{-\mathrm{i}\frac{\pi w}{\lambda f^2}(x^2+y^2)} e^{-\mathrm{i}\frac{2\pi}{\lambda f}(xu+yv)} dx dy,$$
$$(3.5)$$

where the axial coordinate have been replaced with $w = z - 2f$. It has here been assumed that the aperture of the lenses are of sufficient extension to transmit all light diffracted by the SLM. If this assumption is violated, an aperture function must be applied to $U_l(u', v', f)$ before the second Fresnel transform is evaluated, causing a vignetting effect on the trap intensities.

3.1.4 Constructing a Simple Hologram

For numerical propagation, the expression in equation 3.5 is discretized with a sample position spacing corresponding to the pixel size of the SLM. Since the phase of the field in the target positions is generally of no importance, phase terms independent of x and y can be dropped and a simplified expression,

$$U_t(u_m, v_m, w_m) = e^{\mathrm{j}\frac{2\pi w_m}{\lambda}} \sum_{x,y} U_{SLM}(x, y) e^{-\mathrm{j}\left(\frac{\pi w_m}{\lambda f^2}(x^2+y^2) + \frac{2\pi}{\lambda f}(xu_m+yv_m)\right)}, \qquad (3.6)$$

is obtained, here omitting a normalization factor. The subscript m enumerates the target spot positions. The inverse of equation 3.5 yields a similar expression,

$$U_{SLM}(x, y) = \sum_m U_t(u_m, v_m, w_m) e^{\mathrm{j}\left(\frac{2\pi w_m}{\lambda} + \frac{\pi w_m}{\lambda f^2}(x^2+y^2) + \frac{2\pi}{\lambda f}(xu_m+yv_m)\right)}, \qquad (3.7)$$

which can be used for propagation *from* the target spot positions *to* the plane of the SLM. Since the magnification factor given by the lens L2 and the microscope objective is omitted here, the coordinates (u, v, w) must be scaled accordingly.

A simple hologram can be constructed by applying equation 3.7 once to some choice of $U_t(u_m, v_m, w_m)$, where $|U_t(u_m, v_m, w_m)|^2$ is the desired intensity in the spots and $arg(U_t(u_m, v_m, w_m))$ can be arbitrarily chosen. This method is sometimes referred to as the *Lenses & Prisms* (L&P) algorithm, since the two terms in the exponent of equation 3.7 corresponds to the phase shift from a lens and a prism respectively,

$$\varphi_m(x, y)^{lens} = \frac{\pi w_m(x^2 + y^2)}{\lambda f^2}, \tag{3.8}$$

$$\varphi_m(x, y)^{prism} = \frac{2\pi(ux + vy)}{\lambda f}. \tag{3.9}$$

This was the method originally used for constructing phase only holograms [25]. For holograms producing more than one spot, the squared modulus of the field obtained from the L&P algorithm, $|U_{\text{SLM}}(x, y)|^2$, does generally not correspond to the intensity distribution of the illuminating laser beam. The use of phase-only modulating SLMs for realizing such holograms causes reconstruction errors, comprising a large number of so called ghost- or noise orders [26, 27]. The ghost orders interfere with the desired spots and cause errors in the intensity distribution. The problem is particularly pronounced for spot arrangements with certain types of symmetries where the strongest ghost orders overlap with the desired spot positions [28].

3.2 Optimization Algorithms

The ghost orders discussed in the previous section typically degrades the performance of the hologram in terms of *diffraction efficiency* and *uniformity*, two measures that will be used for evaluating hologram generating algorithms throughout this chapter. The diffraction efficiency, e, describes how large fraction of the light that appears in the desired spot positions and is here defined as

$$e = \frac{\sum\limits_m I(u_m, v_m, w_m)}{\sum\limits_{x,y} I(x, y)}, \tag{3.10}$$

where $I(u_m, v_m, w_m) = |U(u_m, v_m, w_m)|^2$ is the obtained intensity in m:th target position and the $I(x, y) = |U(x, y)|^2$ is the intensity distribution of the illuminating laser in the plane of the SLM. The uniformity, u, is a measure of how well the light distributed among the desired spot positions agrees with the desired intensity values and is defined as

$$u = 1 - \frac{max\left(I(u_m, v_m w_m)/I_{d,m}\right) - min\left(I(u_m, v_m w_m)/I_{d,m}\right)}{max\left(I(u_m, v_m w_m)/I_{d,m}\right) + min\left(I(u_m, v_m w_m)/I_{d,m}\right)}, \tag{3.11}$$

where $I_{d,m}$ is the desired intensity in the m:th target position. To increase u and e, several algorithms have been developed that optimizes holograms so that the ghost orders interfere with the spots in a favorable way. The two main groups of such algorithms are based on *simulated annealing* and the *Gerchberg-Saxton* (GS) algorithm respectively. Due to its superior computation speed, only the latter will be treated in this work.

3.2.1   The Gerchberg-Saxton Algorithm

The GS algorithm is named after R. W. Gerchberg and W. O. Saxton [29], who presented it as a method for determining the phase of a wave using measurements of its intensity distributions in the diffraction- and imaging planes. A similar algorithm, used for constructing a diffuser for uniform illumination of hologram recording media was patented by IBM one year earlier [30]. It was later suggested that similar methods could be used for manufacturing *kinoforms* and for interferometric measurements in astronomy [26,31]. Kinoform is the name originally established by IBM in the 1960:s for computer generated phase only holograms [25], in this work simply referred to as holograms. The common task in the various problems where Gerchberg-Saxton algorithms have been applied is to determine unknown properties of a field using measurements or *a priori* determined constraints on other properties of the field, in either one or both of two different planes. This is achieved by numerically propagating the field back and forth between the planes, and after each propagation adjusting the field to comply with the set conditions.

In our problem, designing a phase modulating hologram that produces a limited number of spots in the trapping field, the constraints are applied on the amplitude of the field. In the plane of the SLM, the amplitude is dictated by the illuminating laser, labeled $A_{laser}(x, y)$ and usually having a Gaussian profile. In the trapping field, we set the amplitude, $A_d(u, v, w)$, to a desired value in the spot positions and zero everywhere else. The phase of the field, however, both in the plane of the SLM and the trapping field, is our unknown entity that is to be determined by the GS algorithm. The following steps, also presented as a flow chart in figure 3.2, constitute a standard GS algorithm:

1. An initial field is first created by combining $A_{laser}(x, y)$ with a random phase in the plane of the SLM, $\phi_0(x, y)$: $U_0(x, y) = A_{laser}(x, y)e^{j\phi_0(x,y)}$.

2. The field is propagated to the trapping field to obtain
   $U_n(u, v, w) = A_n(u, v, w)e^{i\phi_n(u,v,w)}$.

3. $A_n(u, v, w)$ is replaced with the desired amplitude, $A_d(u, v, w)$, to obtain
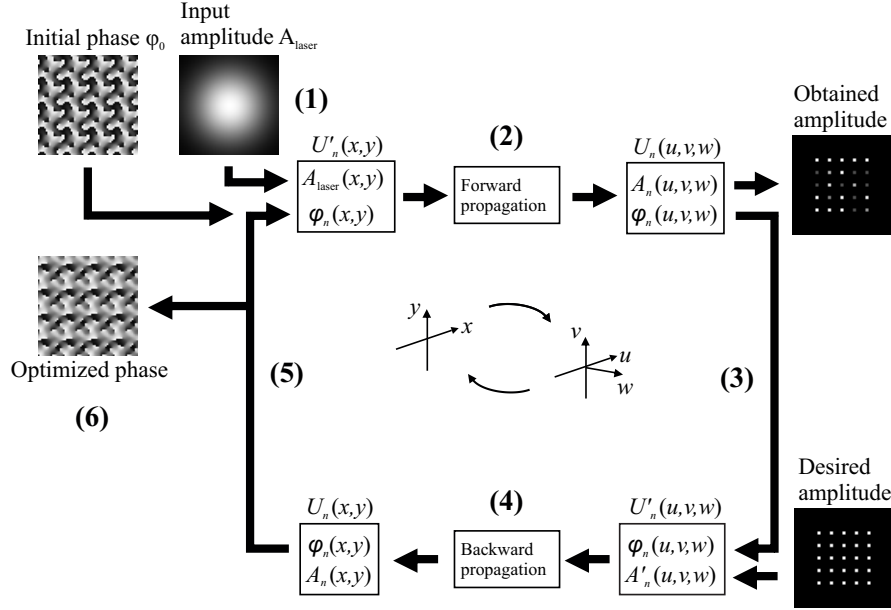 $U'_n(u, v, w) = A_d(u, v, w)e^{j\phi_n(u,v,w)}$.

Figure 3.2: Flow chart describing the standard Gerchberg-Saxton algorithm. The initial field (1) is numerically propagated (2) to the trapping field where the obtained phase is combined with the desired amplitude pattern (3). The field is thereafter backwards propagated and the obtained phase is combined with the amplitude of the incident field (5). The iteration cycle is repeated until the obtained amplitude of the trapping field is sufficiently similar to the desired one. The phase used in the last iteration is then the optimized hologram (6).

4. The field is propagated back to the plane of the SLM to obtain $U_n(x, y) = A_n(x, y)e^{i\phi_n(x,y)}$.

5. $A_n(x, y)$ is replaced with the amplitude of the incident beam, $A_{laser}(x, y)$, to obtain $U'_n(x, y) = A_{laser}(x, y)e^{i\phi_n(x,y)}$.

6. Steps 2-5 are repeated for a predetermined number of times or until $A_n(u, v, w)$ is sufficiently similar to $A_d(u, v, w)$.

7. $\phi_n(x, y)$ from the last iteration is now the phase of our optimized hologram.

The method is sometimes referred to as the *error reduction algorithm*, as it has been shown that the reconstruction error decreases monotonically over the iterations [29]. The error typically decreases rapidly during the first few iterations and the algorithm gives holograms with both improved diffraction efficiency and uniformity compared to the L&P algorithm. After the initial improvement, however, convergence is very slow and the final result usually still suffers from less than optimal uniformity. To improve convergence, various adjustments to

the original GS algorithm have been suggested. In most cases, the improvement is applied in the third step of the algorithm. Instead of replacing the obtained amplitude with the desired one, $A_d(u, v, w)$, a new amplitude, $A'_n(u, v, w)$, is constructed using a weighted combination of the desired and the obtained amplitudes. A flowchart for the modified GS algorithm is shown in figure 3.3. A few different methods for calculating $A'_n(u, v, w)$ are presented in the following sections.

3.2.2   The Adaptive Additive Algorithm

A commonly used modification is the *adaptive additive* (AA) algorithm [32], where the amplitude is replaced with

$$A'_n(u, v, w) = \alpha A_d(u, v, w) + (1 - \alpha) A_n(u, v, w). \tag{3.12}$$

The weight parameter α may be set in the interval $0 \leq \alpha \leq 2$. Using $\alpha < 1$ typically increases the diffraction efficiency compared to GS while the uniformity decreases, using $\alpha > 1$ gives the opposite result while using $\alpha = 1$ takes us back to GS. When used for hologram optimization, the method is equivalent to the *input-output algorithm* [33].

3.2.3   The Generalized Adaptive Additive Algorithm

A variation of the AA algorithm was presented by Curtis *et al.* [34] who instead suggests using

$$A'_n(u, v, w) = \alpha A_d(u, v, w)^2 / (A_n(u, v, w)) + (1 - \alpha) A_d(u, v, w). \tag{3.13}$$

The method has later been referred to as the *generalized adaptive additive* (GAA) algorithm [35].

3.2.4   The Farn Algorithm

A different type of weighting was introduced by M. W. Farn, who instead of calculating $A'_n(u, v, w)$ using the static weight parameter α, used a dynamic and spatially varying weight function, $A'_n(u, v, w) = w_n(u, v, w)$ [36]. In each iteration, $w_n(u, v, w)$ is adjusted according to the ratio of the desired and obtained intensities in each spot raised to the power of a gain parameter, γ. A normalization parameter is also used to prevent divergence of $w_n(u, v, w)$. Rewriting the equations used in [36], $w_n(u, v, w)$ for the n:th iteration is calculated as

$$w_n(u, v, w) = w_{n-1}(u, v, w) \left[\frac{A_d(u, v, w)^2}{A_{n-1}(u, v, w)^2} N_n \right]^\gamma, \tag{3.14}$$
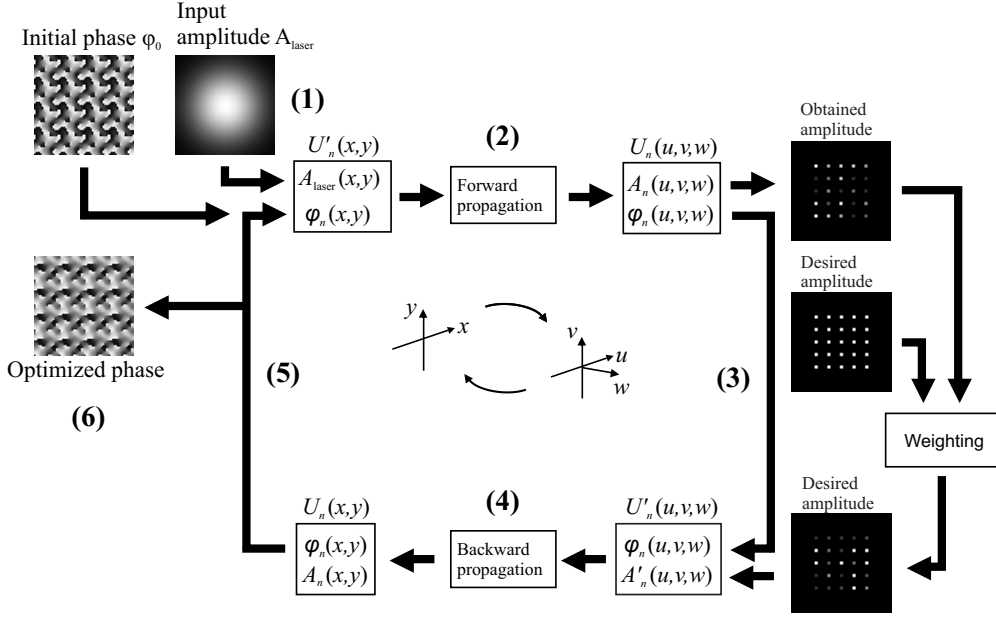
Figure 3.3: Flowchart of a GS algorithm modified to include a weighting step. After propagation to the trapping plane (2), a new field is constructed using the obtained phase and a weighted combination of the desired and obtained amplitude (3). Methods for obtaining the modified amplitude are described in sections 3.2.2–3.2.4. The other steps are identical to the standard GS algorithm (figure 3.2).

where $N_n = \sum_{u,v,w} A_{n-1}(u,v,w)^2 / \sum_{u,v,w} A_d(u,v,w)^2$ is the normalization parameter. This method, here referred to as the *Farn algorithm*, leads to significantly improved uniformity compared to previous methods. In many cases, almost perfect uniformity is reached after only 10 iterations. The diffraction efficiency is generally slightly lower compared to AA and GAA but the difference is usually negligible. A similar method was introduced by J. Bengtsson [37], without the normalization parameter. Di Leonardo *et al.* [35] later suggested using

$$w_n(u,v,w) = w_{n-1}(u,v,w) \frac{\langle A_{n-1} \rangle}{A_{n-1}}, \tag{3.15}$$

where A_{n-1} is the average of the obtained amplitudes. This is of course equivalent to using Farn with $A_d(u,v,w) = 1$ and $\gamma = 0.5$. Although N_n is replaced with $\langle A_{n-1} \rangle^2$, the results of the methods are identical, the choice of normalization parameter has no impact on the convergence of u and e as long as $w_n(u,v,w)$ does not diverge and causes round-off errors.
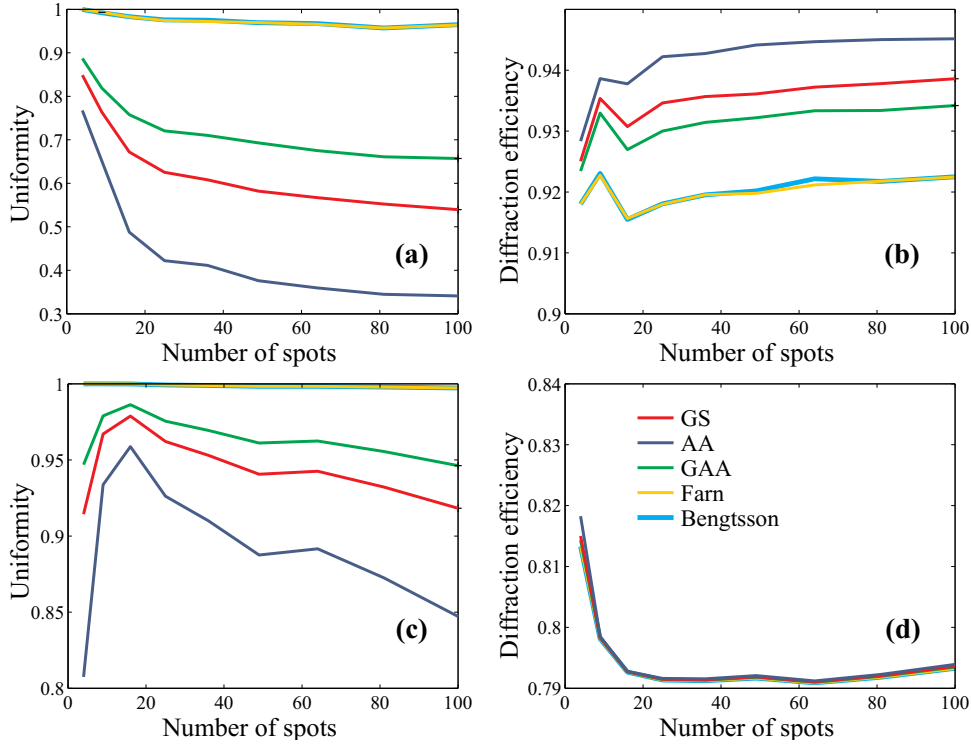
Figure 3.4: Comparison of the uniformity (a and c) and diffraction efficiency (b) and (d) of holograms generated with five variations of the Gerchberg-Saxton algorithm as function of the number of spots produced by the hologram. In (a) and (b), spots were positioned in a square grid with a grid spacing of 16 spot sizes. In (c) and (d), spots were given a small random displacement from the grid. Amplitudes were randomly chosen in a range of 0.5 to 1.5 (arbitrary units).

3.3   Comparison of the Algorithms

Figure 3.4 shows the performance of the described methods in terms of uniformity and diffraction efficiency. The results shown are the average uniformity and diffraction efficiency for 200 holograms generated with each method. For the AA and GAA methods, $\alpha = 0.5$, and for Farn and Bengtsson, $\gamma = 0.5$. As seen in figure 3.4, the methods using dynamic weighting, i.e., Farn and Bengtsson, give far superior uniformity compared to the other methods while the diffraction efficiency is slightly lower. It can also be noted that the holograms where spots are positioned on a symmetric grid are harder to optimize in terms of uniformity, but yields much better diffraction efficiency. This effect can be understood by observing the positions of the ghost orders, which in the symmetric patterns coincide with the spot positions. Those patterns are therefore much more sensitive to the relative phases of the spots since they determine how the spots interfere with the ghost orders.

3.4 Numerical Propagation Methods

The numerical propagation method presented in section 3.1.4 has been used in most implementations and modification of the GS algorithm in this work. It is, however, sometimes more efficient to use *fast Fourier transforms* (FFTs). The appropriate choice of propagation method depends on the application at hand. The FFT is limited to a discrete grid of sampling points whose spacing can only be reduced by increasing the computation window, resulting in increased computation time. The FFT also gives the field in a single plane only. If these limitations are acceptable, however, the FFT is an extremely computationally efficient method for obtaining the field in the entire Fourier plane. It is therefore ideal for situations where a large number of traps are located in the same plane, since the computation time of the FFT is independent of the number of traps. The method presented in section 3.1.4 can be used to calculate the field at any position in space, provided that the Fresnel approximation is valid. The sum only provides the field in one point and the calculation hence has to be repeated for each spot. For a very small number of spots, it is faster than the FFT but as its arithmetic complexity (although not necessarily the required computation time) scales linearly with the number of spots, its efficiency is surpassed by the FFT even for a relatively low number of spots.

3.5 SLM Pixelation

When propagating the field numerically, the sample spacing in the SLM plane is chosen to coincide with the pixel size of the SLM, i.e., only one sample point per pixel is used. This causes higher order spots, in reality appearing outside the computational window, to contribute to the calculated spot intensities by *aliasing*.

If the phase is assumed to be constant across the area of each pixel, the real intensities can easily be calculated when generating the hologram to obtain better uniformity. The pixelated SLM can be seen as the convolution of a grid of point sources, representing the discrete sample points, and a square aperture, representing the pixel geometry. The intensity in the trapping field given by the discrete Fourier transform is therefore modulated by a squared sinc function, the Fourier transform of a rectangular aperture, with minima at the double maximum spot displacement:

$$I_{real}(u,v) = I_{FFT}(u,v) sinc^2 \left(\frac{u}{2u_{max}} \right) sinc^2 \left(\frac{v}{2v_{max}} \right). \qquad (3.16)$$

Here, u_{max} and v_{max} are the maximum spot displacements from the optical axis in u and v direction respectively and $I_{FFT}(u,v)$ is the intensity obtained when
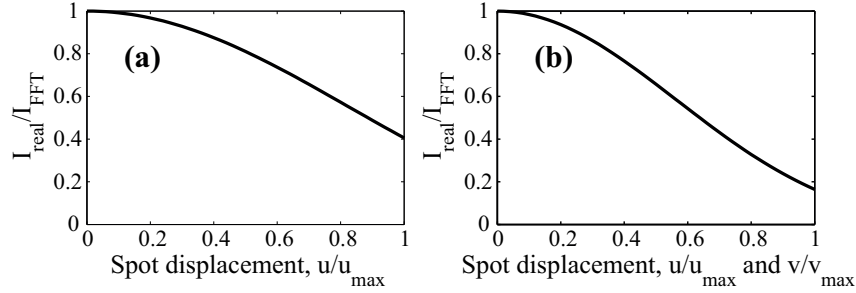
Figure 3.5: Intensity loss in the target position, due to the pixelation of the SLM, as function of displacement from the center in one direction (a) and both directions (b). The plot shows the fraction of the intensity obtained when calculating the farfield intensity using a discrete Fourier transform that is obtained when the hologram is displayed on an ideal but pixelated SLM. The values on the x-axis are normalized to the maximum displacements.

propagating the field numerically.

As shown in figure 3.5, the intensity drops from $I_{FFT}(u, v)$ at the center of the trapping field to $0.405 I_{FFT}$ at maximum displacement along one dimension. For maximum displacement in both u and v direction the obtained intensity is $0.164 I_{FFT}$. By dividing the desired spot intensities with the squared sinc functions before hologram generation, the effect can be canceled. Diffraction efficiency, however, may only be improved by restricting spot positions to have a steering angle much smaller than the maximum possible steering angle.

3.6 Dummy Areas in GS Algorithms

The optimization algorithms presented so far are all designed to optimize both spot uniformity and diffraction efficiency of the holograms. However, maximal diffraction efficiency may not always be desired. A more common requirement is that the spot intensities are kept constant upon changing their arrangement or when adding and removing other spots. The two optimization criteria are often in conflict since the maximum diffraction efficiency usually differs for different spot arrangements. This is partly due to the pixelation effect described in section 3.5, and partly due to interference with ghost orders. It can therefore be advantageous to use a higher total optical power and deliberately distribute some of the light to other positions than the spot positions. A modified GS algorithm is presented in Paper IV, where some of the light can be directed to *dummy areas* in order to maintain control of intensities when repositioning spots. The dummy areas are regions in the Fourier plane of the SLM where the field is allowed to vary freely throughout the GS iterations, both in am-
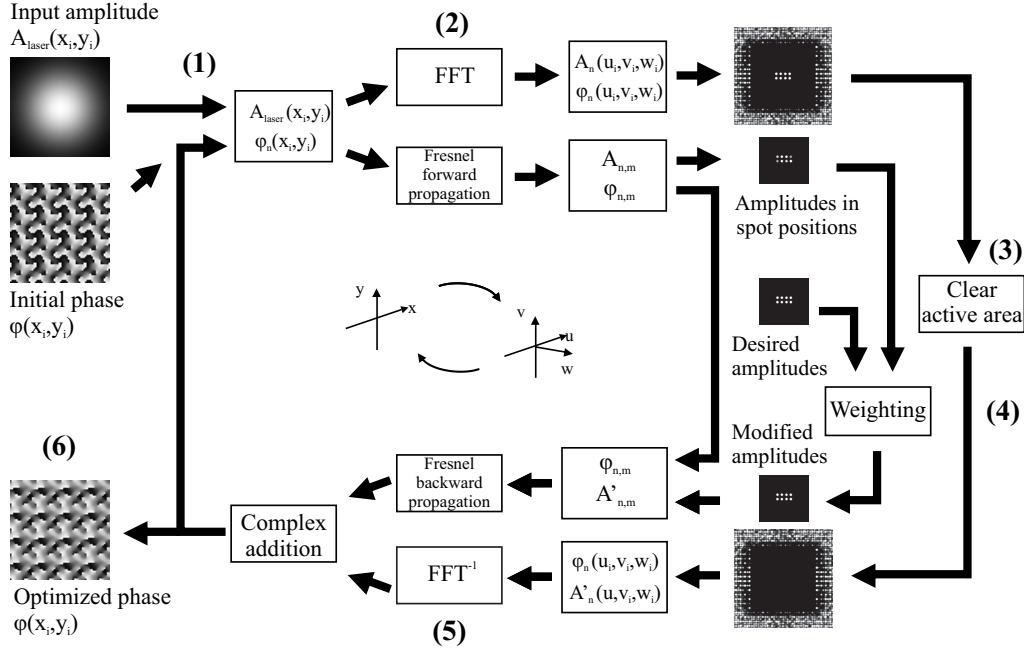
Figure 3.6: Flowchart of a modified GS algorithm using dummy areas. The field in the dummy areas is computed by a separate FFT, the active region is cleared and the remaining field is propagated back to the plane of the SLM, where it is added to the field propagated back from the spot positions.

plitude and phase. The algorithm can thereby better adjust the hologram in order to provide the desired field in the *active region*, the central region around the Fourier plane of the SLM where the desired spots are positioned. For GS algorithms based on FFT propagation, the only modifications required for using the method are removal of the normalization factor in equation 3.14, so that

$$w_n(u, v, w) = w_{n-1}(u, v, w)\frac{A_d}{A_{n-1}}, \tag{3.17}$$

and that the part of the Fourier plane selected as the dummy area is left unaltered when updating its amplitudes in the iteration cycle. For GS using Fresnel propagation, the field in the dummy areas is computed separately using an FFT, and its inverse transform is added to the hologram after propagation back from the target positions. A flowchart of a modified GS algorithm using Fresnel propagation is shown in figure 3.6.

Dummy areas have previously been used to reduce noise in holographic imaging systems [38, 39]. In HOT applications, the benefits are better control of the spot intensities and a drastic reduction of ghost orders normally appearing around the spot arrangement. Excess light is instead directed to the dummy

areas, which can readily be blocked in a conjugate plane outside the microscope.

Results

Figure 3.7 shows holograms (a–c) and corresponding spot patterns (d–f) generated with the modified algorithm directing different amounts of light to the spot positions. The intensity of the spot patterns were calculated as the squared modulus of the Fourier transform of the holograms. Note that the given amount of light directed to the spot positions are the *requested* amount, the obtained percentage is limited by the maximum diffraction efficiency for the spot configuration. When 100% of the available light is requested to the spot positions, the algorithm gives identical results to a weighted GS algorithm without the modification.
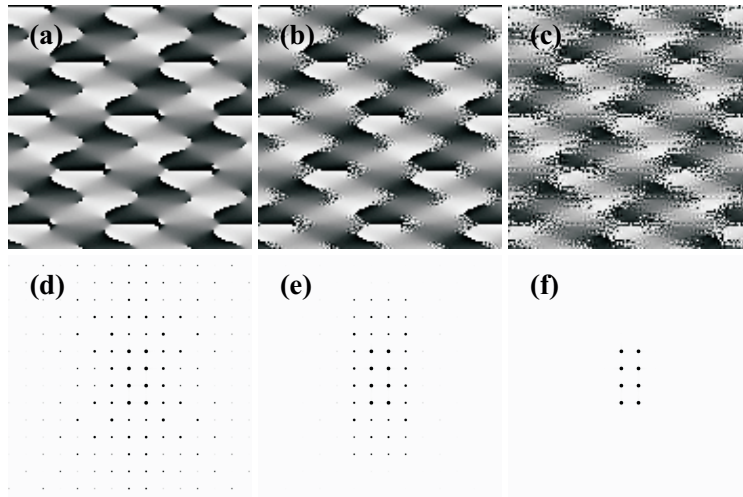
Figure 3.7: Holograms (a–c) and corresponding spot patterns (d–f) generated with the modified algorithm. 100%, 80% and 56% of the available light requested to the eight spot positions in (a) and (d), (b) and (e), and (c) and (f) respectively. The images have been normalized to get equal values in the spot positions and are saturated to better reveal the ghost orders.

Figure 3.8 shows the measured intensities of three diffraction spot as one spot is moved across a ghost order. The figure shows that when most of the light is requested to the spot positions, the intensity of all three spots are subject to large variations when one is crossing a ghost order. By directing 60% of the available light to dummy areas, the variations can be almost eliminated, as shown in figure 3.8 (b). The intensities of the spots were measured by imaging their reflections onto a CMOS camera (MC1362, Mikrotron GmbH), and summing the pixel values in small regions containing each spot.

Further benefits from the use of dummy areas are that spots can be added and deleted without changing the intensity in the remaining spots, and that the intensity of each trap can be controlled independently of other traps. A more detailed description and further results are presented in Paper V.

Figure 3.8: Measured spot intensities in three spot positions as one of them is moved across the position of a ghost order, corresponding to the center of the horizontal scale. The peaks at the bottom of the figures show the measured intensity of another adjacent ghost order.
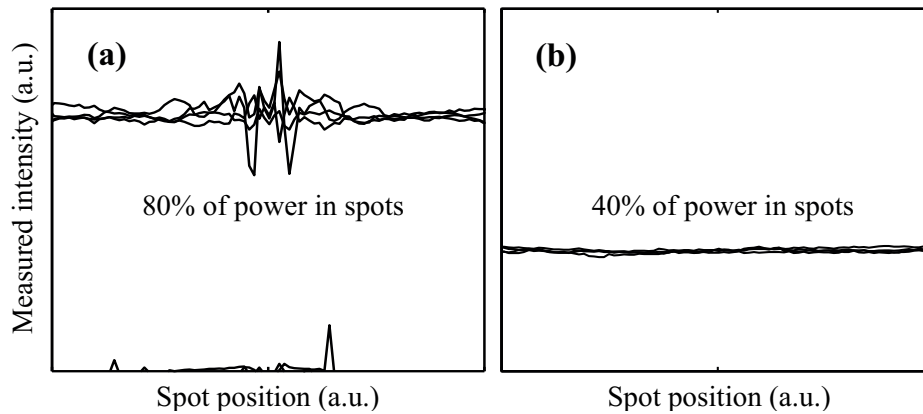
Chapter 4

Liquid Crystals

L iquid crystal (LC) materials are considered from two different perspectives in this thesis. First as the active material in the spatial light modulators used in HOT, which are described in chapter 5, and secondly in studies of its more fundamental properties, described in chapter 8. This chapter provides a brief review of the concepts further discussed in chapters 5 and 8. Liquid crystals is a class of materials that each can simultaneously exhibit the viscous properties of a liquid, and some macroscopic anisotropy, like a crystalline solid. They constitute a broad range of materials, with differently shaped molecules and different types of positional and orientational order. For *thermotropic* LC, the common denominator is the appearance of at least one additional phase between the solid and ordinary liquid (isotropic) phases on the temperature scale. In such phases, a tendency for the molecules to align in certain ways relative to their surrounding causes a long range order, which can manifest in optical properties such as birefringence and optical activity. The LC materials considered in this work all consist of rod shaped molecules and appear in *nematic* or *chiral nematic* phases, the abbreviation LC henceforth refers to such materials only.

4.1   Nematic LC

In the nematic phase, the LC molecules have no positional order, and can diffuse as in an ordinary liquid, but tend to align their long axes with regard to neighboring molecules, giving a long range orientational order and hence optical anisotropy. The local average orientation of the molecules is called the *director*, denoted by the unit vector $\hat{\mathbf{n}}$ and constituting the *director field* $\mathbf{n}(\mathbf{r})$. In the *ground state*, i.e., in the absence of external forces influencing the director field, nematic LC materials are uniaxially birefringent. The refractive indices for light with polarization parallel and perpendicular to $\hat{\mathbf{n}}$, are denoted n_e and n_o respectively. For light traveling at a tilted angle θ_p relative to $\hat{\mathbf{n}}$, the polarization component in the plane of $\hat{\mathbf{n}}$ and the direction of propagation

experience an *effective refractive index*

$$n_{eff} = \frac{n_e^2 n_o^2}{n_e^2 cos^2\theta_p + n_o^2 sin^2\theta_p}. \tag{4.1}$$

4.2 Chirality

Some LC materials have a helically twisted structure of the director field, caused either by chirality in the constituting molecules or by the the addition of a chiral dopant. In the nematic phase, such a material is called a chiral nematic or *cholesteric* LC (CLC). CLCs exhibit optical activity in the ground state, i.e., the ability to rotate the polarization direction of linearly polarized light traveling along the helical axis. The distance required for a 2π rotation of $\hat{\mathbf{n}}$ along the helical axis is called the pitch p of the material. CLC materials are commonly used in *liquid crystal displays* (LCDs) and are studied in the experiments presented in chapter 8.
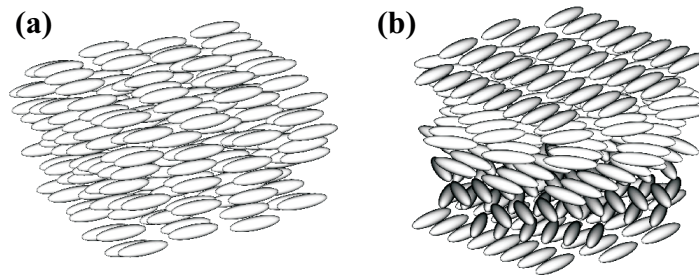
Figure 4.1: Illustration of the alignment of molecules in a nematic (a) and cholesteric (b) LC material. The height of the cut out in (b) corresponds to the pitch of the material.

4.3 The LC cell

When studied or used in practical applications, the LC material is usually sandwiched between two substrates with a separation of a few micrometers. This construction is called an *LC cell*. Close to the substrates, surface interaction causes molecules to align in specific directions, described by the polar and azimuthal angles θ_n and ϕ_n of the director. For amorphous substrates, such as glass, only the polar angle is specified by the surface interaction. To control both θ_n and ϕ_n, e.g., in order to give the cell specific optical properties, an *alignment*

layer is used, usually a mechanically processed polymer. A uniformly birefringent LC cell is obtained when nematic LC is contained in a cell with parallel alignment, i.e., with the alignment layers of the two substrates having the same azimuthal orientation.

If the forced alignment does not correspond to the natural orientation of the molecules, the elastic energy increases as the director field is deformed. The director field then adopts a configuration minimizing the elastic energy in the material. A common example is the twisted nematic (TN) cell, commonly used in LC displays, where a *twist* deformation is given to the director field of a nematic material, by forcing perpendicular alignment at the opposite surfaces of an LC cell. Twist is one of three possible deformations appearing in LC materials, the other two being *splay* and *bend* [40].

4.4 Electro-Optical Modulation

In the presence of an electric field, LC molecules tend to align in the direction of the field, due to induced molecular dipole moments. In an LC cell, the torque exerted by the external field is balanced against the elastic forces caused by deformations near the alignment layers. The orientation of $\hat{\mathbf{n}}$ can therefore be controlled by varying the field strength. This changes the optical properties of the material, allowing for electro-optical light modulation. The field is applied using transparent, usually indium tin oxide (ITO), or reflective electrodes covering the cell substrates. Applying an electric field across a parallel aligned NLC cell changes the polar angle of the director, θ_n, and thus also n_{eff}. Such device can be used as a variable phase retarder, since the optical path length through the cell changes with n_{eff}. The principle is illustrated in figure 4.2.

If the electric field is perpendicular to the director, the torque on the molecules is zero. It is therefore common to induce a *pretilt* to the boundary layers, denoted θ_0 in figure 4.2 (a), to obtain a faster response to applied fields and to predefine the direction of the torque.
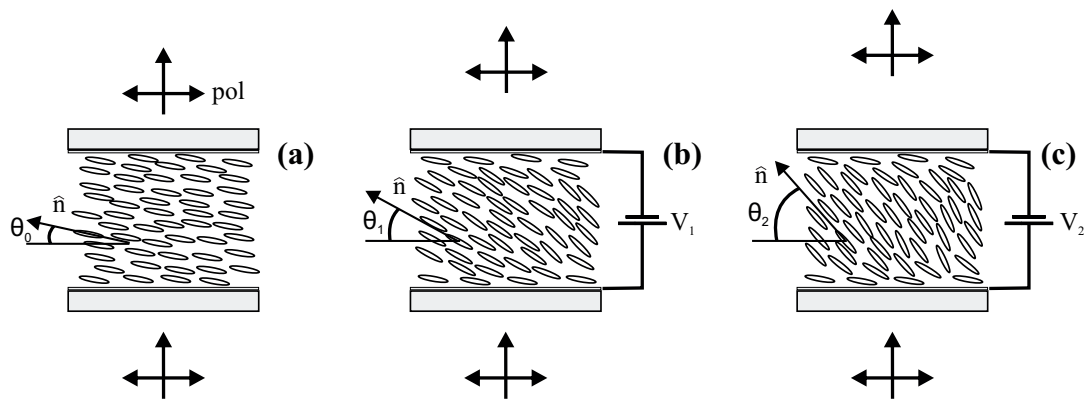
Figure 4.2: Cross section of a parallel aligned NLC cell with pretilt θ_0 (a). (b) and (c) show the same cell with applied voltages V_1 and V_2, where $V_1 < V_2$, tilting the director to θ_1 and θ_2 respectively. The refractive index for light with polarization, indicated with horizontal arrows, in the direction of the alignment layers changes with θ, so that propagation is faster for high voltages.

Chapter 5

Spatial Light Modulators

T he spatial light modulators used in HOT are typically LC based phase re-
tarders, utilizing the technique described in section 4.4, where the phase
retardation of a reflected laser beam can be locally assigned from a computer in
a 2D array of pixels. Phase patterns generated using the methods described in
chapter 3 can be physically realized with such devices if each pixel can provide a
phase retardation in a range of 0–2π. However, while the theoretical uniformity
of such hologram can be nearly perfect, and the diffraction efficiency high, such
performance is typically not obtained in reality. LC based SLMs all have limi-
tations causing the realized holograms to differ from the generated ones, which
in turn causes errors in the obtained spot intensities. If the limitations of the
used SLM are known, they can to some extent be compensated for using mod-
ified algorithms for hologram generation and post processing of the generated
holograms.

Three such modifications will be presented in this chapter after a description
of the working principle of the SLMs used in this work. The three methods are
also presented in Paper I, VI and VII.

5.1 Liquid Crystal SLMs Used in this Work

Liquid crystal based spatial light modulators (LC-SLMs) can be either trans-
missive or reflective, and modulate either the phase or polarization state of the
illuminating light. Positioned between polarizers, the latter type can be used for
amplitude modulation and are used in many commercially available projectors.
The LC displays found in other consumer products such as mobile phones and
TV sets can also be referred to as spatial light modulators although the term is
rarely used for such devices. SLMs used in HOT are almost exclusively reflective
and phase modulating. In such SLMs, an NLC material is sandwiched between
two substrates with parallel surface alignment. The front substrate has a single
transparent electrode covering the entire active area, while the rear substrate,

31

the *backplane*, can have a matrix of pixel electrodes or a photoconductive layer in front of a single transparent electrode. When varying the field across the LC material, the molecules are rotated in a plane perpendicular to the substrates. Incident light polarized in this plane experiences different refractive indices depending on the rotation of the director and can hence be given a variable phase shift. Since the type of SLMs described here uses LC materials with no permanent molecular dipole moment, the torque from an applied field does not depend on its polarity. To avoid degradation of the LC material due to ion migration, the polarity of the applied field is switched at a high frequency.

5.1.1   Electrical Addressing

The back plane in *electrically addressed* SLMs typically consists of a silicon substrate covered by an array of reflection coated pixel electrodes. The pixels can be controlled individually following an active matrix addressing scheme, where pixels in each row are updated simultaneously and rows are updated sequentially. For a given maximum voltage available in the backplane electronics, V_{bp}, the common electrode is usually kept at a constant voltage of $V_{ce} = \frac{1}{2}V_{bp}$, while the pixel electrode is rapidly switched with $V_{pe} = V_{ce} \pm V_{pixel}$ to avoid material degradation. V_{pixel} is here the desired voltage across the LC material for the pixel. This gives a usable voltage range of 0 to $\frac{1}{2}V_{bp}$ across the LC material, where V_{bp} is usually 5 V, a standard supply voltage for IC electronics. This addressing scheme is described in figure 5.1 (a) and a schematic crossection of the SLM is shown in 5.2 (a).
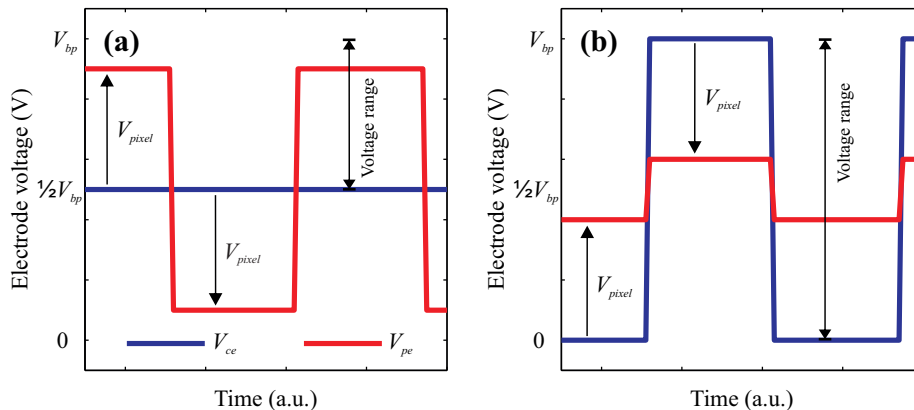

Figure 5.1: Addressing schemes for LCoS SLMs giving a maximum voltage of $V_{bp}/2$ (a) and V_bp (b) across the LC cell.
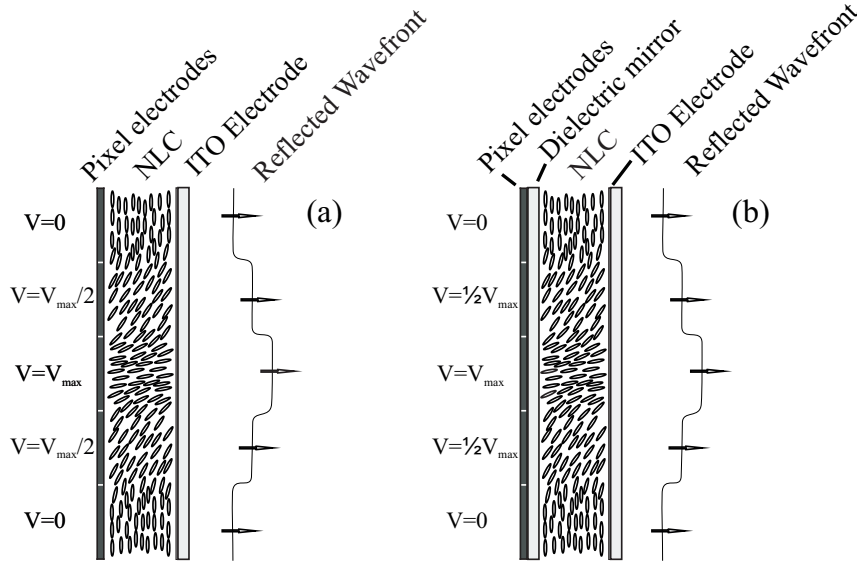
Figure 5.2: Schematic descriptions of two types of SLMs used in this work. (a) shows an electrically addressed reflective SLM and (b) shows a similar SLM with the addition of a dielectric mirror in front of the pixel electrodes. The arrows indicate the propagation direction of a reflected wavefront.

5.1.2 Increased SLM Fill Factor

Ideally, SLMs used for HOT should have short response time and high diffraction efficiency. The response time depends on material properties of the LC, and on the maximum electric field across the material. The diffraction efficiency is determined by the accuracy of the phase modulation and by the *fill factor* of the backplane, i.e., the ratio of the area occupied by reflective material to the total active area of the back plane. To increase the fill factor, the pixelated electrode array is sometimes covered with a dielectric mirror reflecting the optical wavelength for which the SLM is specified, as illustrated in figure 5.2 (b). The increased separation of the electrodes reduces the field across the LC material for a given V_{pixel}, and hence increases the response time unless V_{pixel} can be increased. A straightforward but often costly method to increase the field is to construct backplanes electronics that handle higher than standard voltages. One of the SLMs used in the experiments described in Paper VII, which uses a dielectric mirror for increased diffraction efficiency, instead has an alternative driving scheme which makes use of the full voltage range of the backplane. In this SLM, the voltage on the common electrode is toggled with V_{bp} at a frequency in the kHz range, and the pixel electrodes are switched with the same frequency between V_{pixel} and $V_{bp} - V_{pixel}$, as illustrated in figure 5.1 (b). While this method doubles the available voltage range for a given V_{bp}, and

thus reduces the response time, the active matrix addressing scheme, in which all pixel rows cannot be updated simultaneously, causes a phase difference in the switching of different rows relative to the toggling of the common electrode. This causes the average electric field across the material for a given V_{pe} to vary for different rows, giving a slightly varying phase response across the surface. This issue will be further discussed in section 5.2.2.

5.1.3   Optical Addressing

In optically addressed SLMs, the backplane electrode is not pixelated. Instead, a single electrode is sandwiched between the backplane and a layer of photoconductive hydrogenated amorphous silicon (a-Si:H). An AC-field is applied across the front and back electrodes, and when illuminated, the resistance of the a-Si:H layer drops locally and the field in the LC material increases. The modulator is controlled by projecting an image onto the backplane whose intensity corresponds to the desired phase modulation. One of the SLMs used for experiments presented in Paper I and Paper VI is of this type. In this SLM (PPM X8267-15, Hamamatsu Photonics), illustrated in figure 5.2 (c), the optically addressed phase modulator is bundled with a diode laser illuminating an electrically addressed amplitude modulating SLM, which is imaged onto the a-Si:H layer using a lens arrangement. An advantage of this arrangement is that the backplane can be made very flat to avoid unwanted aberrations induced by the SLM, common for devises using silicon backplanes, and that the lack of pixel structure on the backplane reduces diffraction to higher orders for beam steering applications. A disadvantage is that the double set of LC modulators increases the total response time of the system. The lack of distinct pixel structure is primarily beneficial for phase patterns with slow spatial variations and for single beam deflection, but can induce error in the obtained spot intensities for more complex spot patterns. The projection of the amplitude modulating SLM is limited by diffraction effects in the lens system, which limits the resolution of the phase modulation. This issue will be further discussed in section 5.2.1.

5.2   Correction Methods for LC-SLMs

Some non-ideal behavior of LC-SLMs was mentioned in the previous section; a *spatially varying phase response* can partly be caused by the pixel addressing scheme, as described in section 5.1.2, *crosstalk between adjacent pixels* is present in all LC-SLMs but especially pronounced in the type of SLM described in section 5.1.3, and the *finite response time* was mentioned although its impact on the spot intensities was not clarified. In this section, these factors will
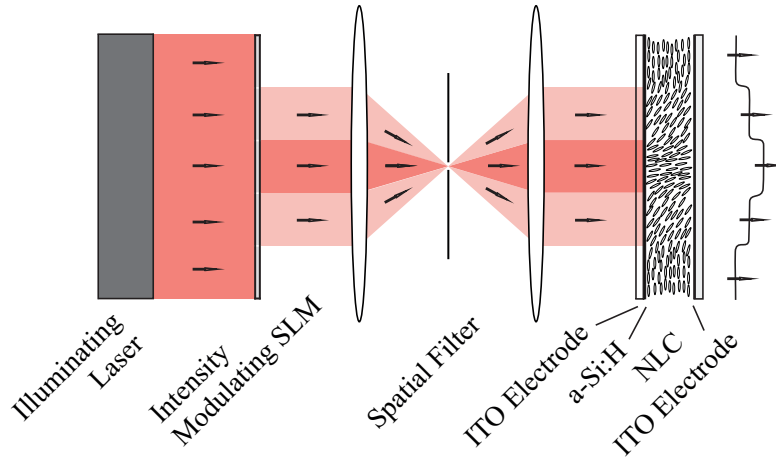
Figure 5.3: Configuration of the optically addressed SLM used in this work. The photoconductive a-Si:H layer of the optically addressed SLM is illuminated by a laser which is spatially modulated by an amplitude modulating SLM. The arrows indicate the propagation direction of a reflected wavefront. The exact lens configuration is undisclosed by the manufacturer.

be further discussed and methods for improving the performance of LC-SLMs described.

5.2.1   Pixel Crosstalk

When calculating holograms, a discrete representation of the phase pattern in the plane of the SLM must be used. It is often assumed that the phase retardation is constant over the entire surface of each pixel and that the pixels are completely independent. Under this assumption, a matrix with the same number of elements as the number of pixels can truly represent the physical phase retardation, and the field in the target positions is given exactly by the numerical propagation of this matrix. For LC-SLMs, however, these assumptions can generally not be fulfilled completely. The phase shift of an SLM pixel is determined by the local orientation of the director of the LC material, which in turn depends on the voltage applied across the material, e.g., using one of the techniques described in section 5.1. Although the electrodes of adjacent pixels may be completely separated on the backplane, the field in the LC material always spreads slightly. This phenomenon is called *fringing fields* and causes crosstalk between pixels [41], as illustrated in figure 5.4. The effect is more pronounced for SLMs with high thickness/pixel size-ratio, e.g., SLMs built for long wavelengths and SLMs with high resolution and small active area. Since the thickness here refers to the distance between the front- and the pixel elec-
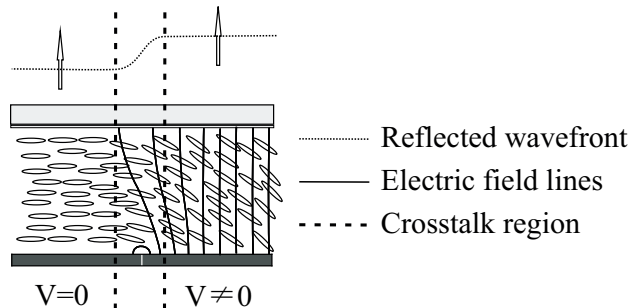
Figure 5.4: Cross section of two adjacent pixels in an LC-SLM. When different voltages are applied to the pixels, fringing fields appear near the border of the pixels and causes crosstalk in the obtained phase modulation of a reflected wavefront.

trodes, the use of a dielectric mirror in front of the backplane also gives a slightly stronger crosstalk. The LC material itself can further cause some crosstalk since the elastic forces in the material prohibits very abrupt spatial variations of the director.

The optically addressed SLM described in section 5.1.3 exhibits much stronger crosstalk than most electrically addressed SLMs. The fringing field effect is present also in this SLM, but the main contribution results from the imaging optics. It is in fact deliberately designed to give strong crosstalk using a spatial filter in the internal lens system, in order to reduce the intensity of higher diffraction orders.

Regardless of its cause, pixel crosstalk results in intensity errors in the target positions when employing the standard methods for hologram generation described in section 3.2. A modified GS algorithm minimizing such errors is presented in Paper VI. The algorithm includes a simplified model of the crosstalk in the iteration cycle so that its effect can be compensated for by the weight function. In this model, we assume that the actual phase retardation realized by the SLM can be calculated from the convolution of the ideal hologram with a kernel function specific for the used SLM. A flowchart of the modified algorithm is showed in figure 5.5. After each numerical propagation back to the plane of the SLM, the phase of the obtained field is calculated and convolved with the kernel function (step 7). When propagated to the target positions, the weighting function, which originally compensated for errors caused by the lack of amplitude freedom in the plane of the SLM, now also compensates for errors caused by the convolution. To more accurately model the crosstalk, which sometimes extends over only fractions of a pixel, the convolution can be performed at a higher spatial resolution than the native resolution of the SLM. An *oversampling* step is then introduced after the backward propagation and
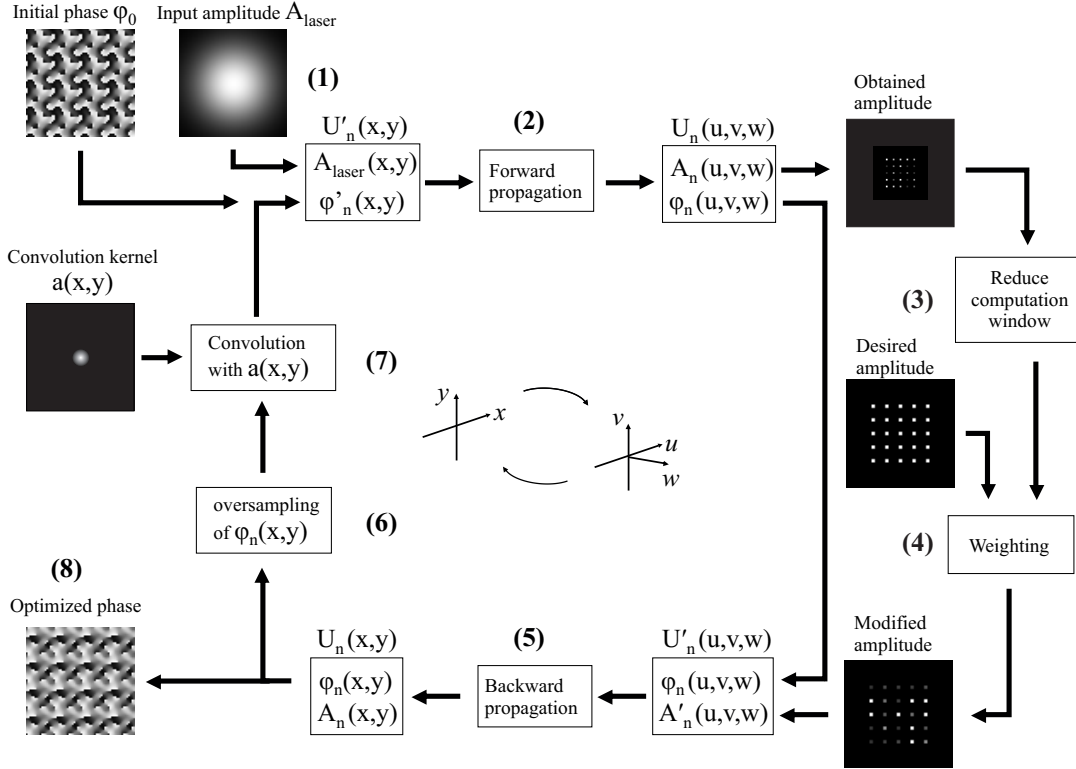
Figure 5.5: Flow chart of a weighted GS algorithm modified to compensate for pixel crosstalk. In addition to the regular steps of the weighted GS algorithm (see figure 3.3), the phase obtained after back propagation (5) is oversampled to a higher resolution than the native resolution of the SLM (6), and convolved with the kernel function $a(x, y)$ (7). After the resulting field has been forward propagated, the obtained trapping field is reduced in size so that the subsequent back propagation has a sample distance that matches the SLM pixel size. The optimized phase (8) is the phase that, after convolution with the kernel function, gives the desired trapping field.

before the convolution in each iteration (step 6). After the forward propagation, the computation window is reduced to again correspond to the resolution of the SLM (step 3).

Accompanying the compensation method, Paper VI also includes a method for finding the optimal kernel function for the used SLM. The method relies on comparison of experimentally observed spot intensities for a large number of one dimensional binary phase gratings displayed by the SLM, with different phase separation and grating period, to calculated spot intensities for the same gratings convolved with different *trial functions*. The used trial functions were

elliptical generalized Gaussians,

$$a_{r_x,r_y,\gamma}(x,y) = exp\left(-\left(\frac{x^2}{2r_x^2} + \frac{y^2}{2r_y^2}\right)^{\gamma}\right), \tag{5.1}$$

whose widths r_x and r_y and *shape parameter* γ were varied until the difference between simulations and measurements was minimized.

Measurements and Results

Measurements for both the kernel optimization and for evaluation of the compensation method were done by focusing the diffracted beam directly onto the CCD sensor of a camera. The spot intensities were measured by summation of pixel values in a small region enclosing each spot, after subtraction of a dark image acquired with the laser light blocked. Measured and simulated results are shown in figure 5.6.

The method was found to drastically reduce spot intensity errors for the optically addressed SLM, the average uniformity was increased from 0.40 to 0.88 for the tested spot arrangements. Beside intensity errors, a common effect of the pixel crosstalk is the appearance of an unwanted zeroth order diffraction spot. For spot arrangements where one spot position coincides with the zeroth diffraction order, its intensity could in many cases be reduced to the desired intensity. For arrangements with no spot positioned in the zeroth diffraction order, its intensity is unaffected by the correction method since is not controlled by the weighting function.

The method rendered similar results with and without oversampling in the convolution step. This somewhat surprising result is attributed to the relatively large range of the crosstalk and lack of sharp features in the hologram realized by our SLM. The exact configuration of the internal imaging system is not disclosed by the manufacturer of the SLM, but it can be expected that the spatial filter causes a close to Gaussian broadening of the intensity pattern on the photoconductive backplane in the SLM, and hence also of the realized phase pattern.

An alternative method for finding the kernel function was tested after publication of Paper VI. In this method, no assumptions were made about the kernel function. It was instead randomly varied pixel by pixel and the difference between the measurements, used in the previous method, and simulations, using the altered kernel, was minimized according to the Monte-Carlo method. The obtained a kernel function suggested that there was astigmatism, i.e., defocusing along one direction, in the internal imaging system of the SLM.
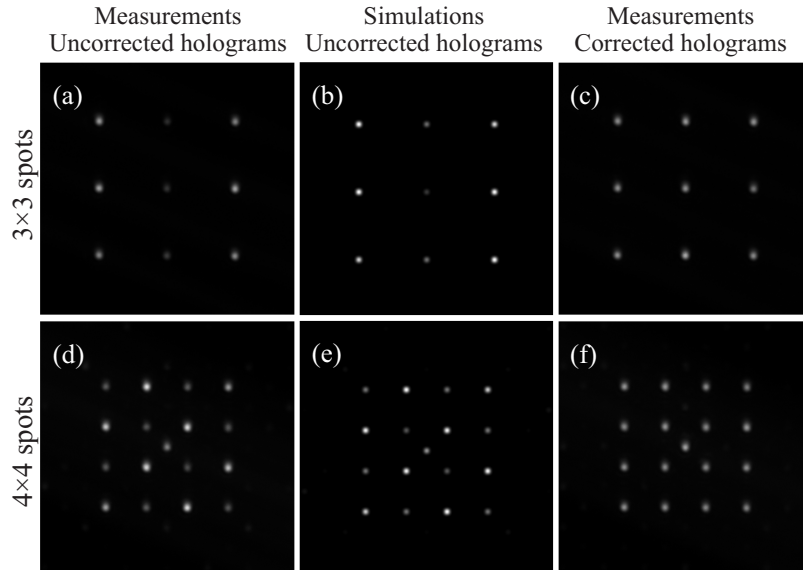
Figure 5.6: Measured (a, c, d and f) and calculated (b and e) spot intensities for hologram generated without (a, b, d and e) and with (c and f) correction for pixel crosstalk. The calculated intensities were calculated from the Fourier transform of the holograms used for (a) and (c) after convolution with the optimized kernel function.

5.2.2   Spatially Varying Phase Response

Before a hologram is displayed on the SLM, the pixel phase obtained from the generation algorithm must be converted into 8 or 16 bit integers, the pixel values, which in turn are converted into pixel electrode voltages by the SLM hardware. In most cases, the conversion is done using a single lookup table (LUT) for all pixels. The LUT is often provided by the SLM manufacturer and sometimes applied in the SLM hardware so that the user can create their holograms assuming a linear phase response. The LUT can also be created and applied by the user themself using a variety of methods [42–45]. It has been shown, however, that the phase responses of pixels at different locations on the SLM are not necessarily equal [46, 47]. The use of a single LUT for the entire SLM can therefore not provide correct conversion for all pixels. This causes errors in the physically realized hologram, which can lead to both decreased uniformity of the obtained intensity of the spots, a stronger zeroth order, and to deformation of the intensity profiles of the individual spots.

We can identify three possible causes for spatial variations in the phase response. First, if the backplane of the SLM is not completely flat, the thickness of the LC cell can vary over the surface. This causes both variations in the obtained electric field across the LC material for a certain pixel electrode voltage,

and differences in the obtained phase retardation for a certain electric field in the material. Second, we have observed that the phase response changes slightly with the optical power of the illuminating laser beam, and that the change varies over the surface of the SLM. A possible reason for this behavior could be that weak absorption in the LC-cell causes local heating of the LC material, varying with the Gaussian intensity profile of the beam. The variations could alter the elastic properties or refractive index of the material and hence give a different phase response. The third observed effect is present in SLMs with the modified electrical driving scheme discussed in section 5.1.2.

By measuring the local phase response for small areas of the SLM and making the phase-pixel value conversion spatially variant, the problem can be reduced. Since it is not feasible to obtain the phase response for each pixel individually, interpolation of the average phase responses of regions containing several pixels must be used. In the method presented in Paper VII, the pixel values are obtained by evaluation of a three dimensional polynomial, whose variables are the spatial coordinates of the SLM, (x, y), and the desired phase, ϕ_{desired}. The polynomial coefficients are determined by fitting to LUTs obtained from 8×8 regions, of 64×64 pixels each. The phase response in each region is obtained by measuring the intensity in the 1:st diffraction order of binary phase gratings, covering only the investigated area, as the difference of the pixel values assigned to the two levels of the binary grating is stepped from 0 to 255. The method is referred to as *spatially variant phase conversion* (SPVC).

Measurements and Results

The performance of the method was evaluated by repeating the measurement of local phase responses after the polynomial conversion, by measuring the spot intensities and the zeroth order intensity for full frame holograms, and by measuring the obtained trap stiffness for full frame holograms. Spot intensities were measured in the HOT system, by placing a mirror in the sample plane of the microscope so that their reflections were imaged onto the camera.

In the trap stiffness measurements, five traps were positioned equidistantly on a line centered on the x-axis with an offset in the z-direction. The positions of silica microspheres, with diameters of 2.56 μm, held in each trap were measured and the trap stiffnesses were determined as described in section 6.3.2. The method was found to improve the uniformity of the obtained trap stiffnesses. Further, a relatively strong zeroth order spot that was observed when using a regular LUT was drastically reduced using the polynomial method. The zeroth order spot was, however, not influencing the stiffness measurements significantly due to the offset in the z-direction. Also the direct measurements of the spot intensities showed a significant reduction of the intensity of the zeroth order spot. Figure 5.7 shows spot patterns from holograms converted with a regular
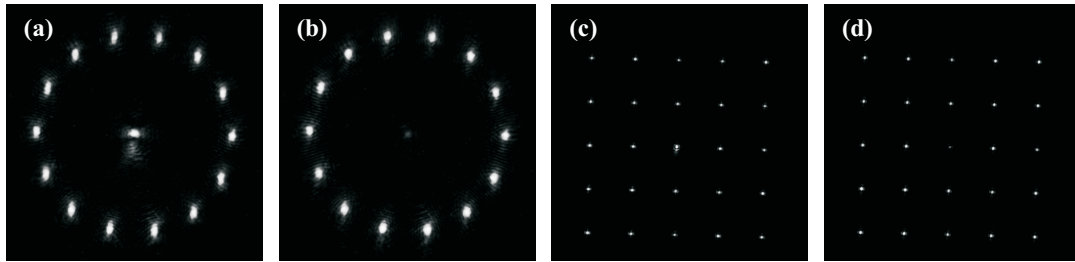
Figure 5.7: Spot patterns from holograms whose phase were converted to pixel values using a single LUT (a and c), or a seventh order three dimensional polynomial (b and d). No spot is intentionally directed to the zeroth order position, around which the patterns are centered.

LUT and with the polynomial method.

More results and a more thorough description of the method is presented in Paper VII. Another method was presented in reference [46], where a single LUT was scaled using a 2D matrix, with one scale factor for each pixel, to accommodate to spatial variations in the phase response. In reference [48], a method similar to ours was presented where *linear interpolation* of LUTs obtained from local phase response measurements, was used.

5.2.3   Intensity Fluctuations During SLM Update

Holograms with high uniformity and controllable diffraction efficiency can be generated with the method described in section 3.6, and adapted to the physical properties of the used SLM as described in sections 5.2.1 and 5.2.2 to obtain a highly controllable trapping field. However, when the SLM is updated to a new hologram, control over the spot intensities may temporarily be completely lost, even if each displayed hologram is highly optimized. All SLMs have a nonzero response time, during which the SLM pixels are reconfiguring to the new setting. Unless the two consecutive holograms are very similar to each other, the SLM therefore undergoes a series of more or less uncontrolled states during the update. And, as a consequence, light is typically directed away from the desired positions. Note that even if the two holograms have similar output fields, perhaps only one of many spots is being slightly displaced, it is probable that the individual pixel settings of the two holograms differ drastically. In OFM applications, this effect prevents accurate measurements on dynamically moving traps or even on stationary traps if the hologram is being updated. In addition, the drop in intensity of the traps during the SLM update may be so severe that trapped objects are lost. An obvious way of reducing the problem would be to use an SLM with very short response time. Ferroelectric Liquid
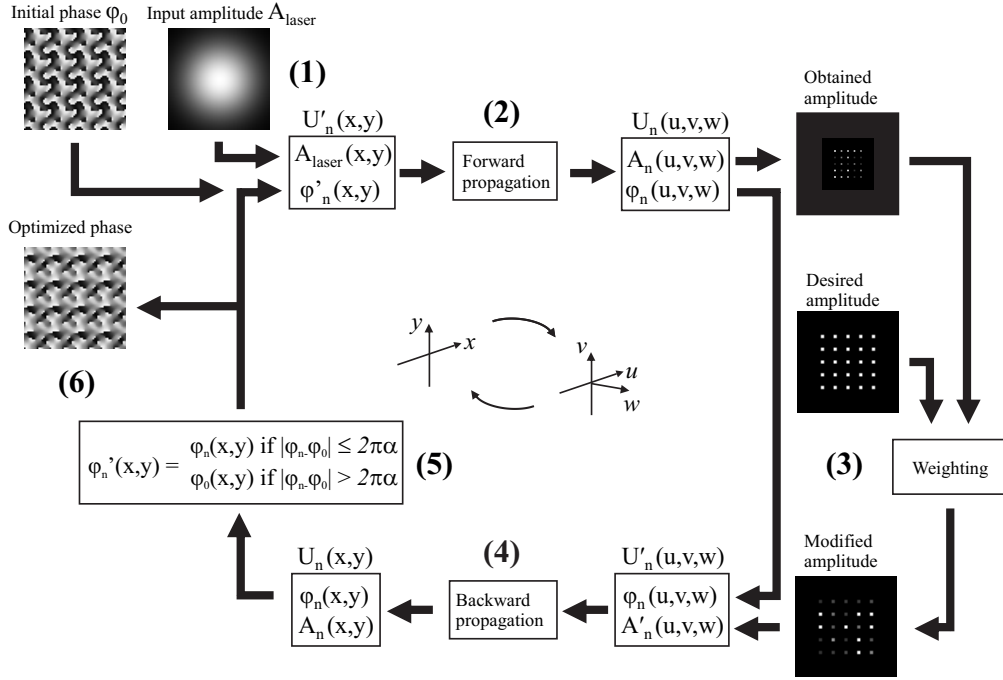
Figure 5.8: Flow chart of the GS-RPC algorithm. A new step (5) is introduced in a weighted GS algorithm that limits the maximum phase change for each pixel compared to the previous hologram. The limit is applied after each iteration cycle and results in a hologram more similar to the previous one.

Crystal (FLC) SLMs are available with a response time in the order of 10-100 μs. With such an SLM, the duration of the intensity fluctuations would be short enough to be considered negligible. However, FLC SLMs typically have binary phase modulation, which result in considerable limitations on the obtainable trapping field. Nematic LC-SLMs used in HOT systems, on the other hand, typically have a response time in the order of 1-100 ms and fluctuations during update cannot be neglected.

For nematic LC-SLMs, the uncontrolled behavior during the response time can instead be reduced by making consecutive holograms more similar to each other. In Paper I, a method that practically eliminates the fluctuations is presented. The method is also summarized here.

The first step towards obtaining more correlated holograms is to set ϕ_0 to be the phase of the previously hologram when constructing the initial field for the GS algorithm (step 1 in figure 5.8). This slight modification generates holograms that significantly reduce the intensity loss during the update, has no effect on the computational complexity and typically increases the convergence speed of the algorithm.

To further reduce intensity fluctuations, the change in phase modulation of a pixel from one hologram to the next can be actively suppressed when generating the hologram. In Paper I, we present a method for achieving this using a modified GS algorithm. After the field has been propagated back to the SLM plane in the algorithm, the phase of each pixel, ϕ_n, is compared to its value in the previous hologram, ϕ_0. Pixels for which the absolute value of the difference between ϕ_n and ϕ_0 exceeds a certain value are reset to their initial value, ϕ_0. The phase used in the next iteration, ϕ'_n, is then

$$\phi'_n(x,y) = \begin{cases} \phi_n(x,y) \text{ if } |\phi_n - \phi_0| \leq 2\pi\alpha \\ \phi_0(x,y) \text{ if } |\phi_n - \phi_0| > 2\pi\alpha, \end{cases} \tag{5.2}$$

where α is set to 0.5–1. This method, named GS-RPC where RPC stands for Restricted Phase Change, forces the algorithm to converge to a hologram that is much more similar to the previous one than with the unmodified algorithm. A flow chart of the algorithm is presented in figure 5.8, where the new step is shown in (5).

Measurements and Results

The performance of the algorithm was tested both in simulations and in experiments. In simulations of the spot intensities during update, intermediate states of the SLM were calculated and the resulting fields propagated to the target positions. The intermediate states were by obtained assuming that the phase modulation of each pixel changes linearly throughout the update and that the total response time is the same for all pixels. Measurements were performed both in a HOT system, where the position of an optically trapped bead subject to an induced constant drag force was measured, and in a free space setup, by measuring the spot intensities using a CMOS camera sensor. In the optical trapping measurements, the position of a silica microsphere in a stationary trap was monitored while other traps were added and removed, and the surrounding fluid moved at a constant speed using a motorized microscope stage. The positions were measured using the method described in section 6.1.2 in the next chapter of this thesis. Results from the trapping measurement are presented in figure 5.9. Comparing (a) and (b) demonstrates the benefit of reusing the previous hologram when constructing the initial field in the algorithm. Comparing (d) and (e) shows that the fluctuations during the updates of the SLM are further reduced when using RPC. The non-transient variations of the beads position, seen in (d) and (e) are likely due to the pixel crosstalk effect, described in section 5.2.1, giving varying errors in the trap intensities for different holograms.

A comparison of three methods for hologram generation using a GS based algorithm is presented in figure 5.10. Spot intensities during update between two

holograms were simulated and measured for holograms generated with weighted GS using random initial field (a and d), using previous hologram for the initial field (b and e) and using GS-RPC (c and f). The trap configuration consisted of 10 spots equidistantly positioned on a circle. In the initial hologram, one spot was removed. In the second hologram, it was replaced and another spot removed. This comparison exemplifies the agreement between simulations and experiment and shows how the intensity fluctuations can be completely removed using our method. Further results are presented in Paper I.
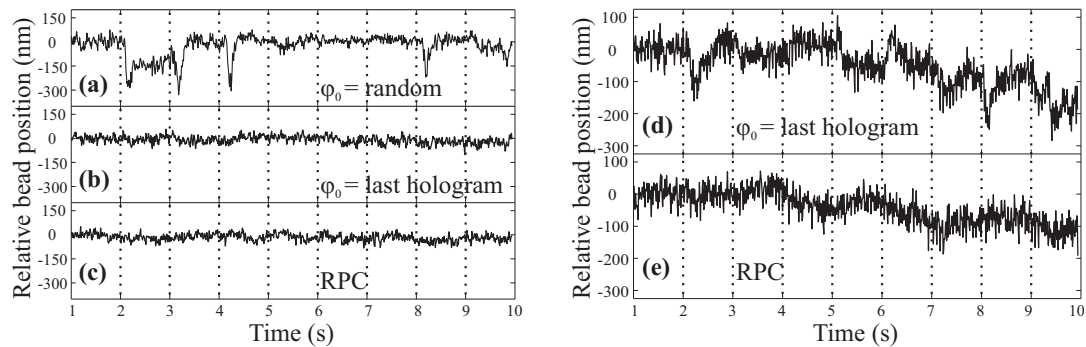
Figure 5.9: Measured positions of an optically trapped silica microsphere subject to a constant viscous drag force, obtained by moving the microscope stage with 20 μm/s (a–c) and 150 μm/s (d and e), while updating the SLM for different trap configurations. Holograms were generated using a GS algorithm with random inital phase (a) or using the previous hologram as initial phase (b and d), and with a modified GS algorithm using RPC (c and e).
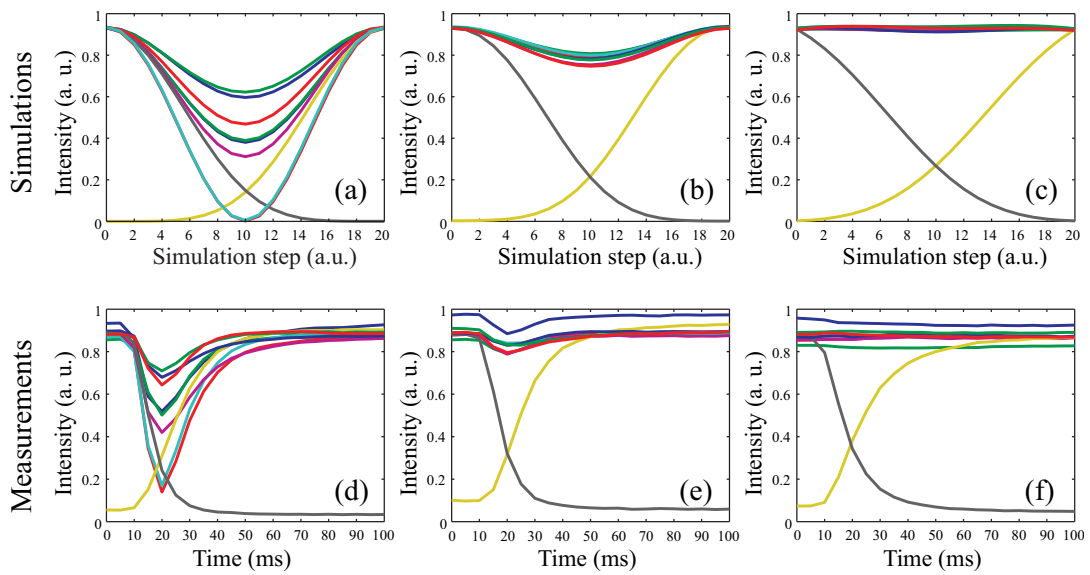
Figure 5.10: Simulated intensities of 10 spots during update from one hologram to another (a-c) and measured intensities during update between the same holograms (d-e). The holograms were generated using a weighted GS algorithm (a and d), the same algorithm using the first hologram as start values when generating the second (b and e) and GS-RPC (c and f). One spot had been removed in the first hologram (low intensity at t=0) and was replaced in the second, where another spot was removed (low intensity at t=100 ms).

Chapter 6

Optical Force Measurement

I n many optical force measurement (OFM) applications, a probe particle with known optical properties and shape is optically trapped and used as a force transducer. Typically, a spherical silica- or polystyrene particle in the size range of one to a few micrometers is used. External forces acting on the probe are determined by measuring its displacement from the equilibrium position in the trap. Within a region close to the equilibrium position, the optical force is proportional to the displacement and hence follows Hooke's law; $F = -\kappa x$, where κ is the *spring constant* and d denotes the displacement from the equilibrium position. If the spring constant, usually referred to as the *trap stiffness* in optical trapping, is determined, the force exerted on the probe particle can therefore be calculated from position measurements. Even though the trap stiffness in principle can be calculated theoretically [49, 50], the errors induced by uncertainties in particle size, light intensity and shape of the focal volume, can be significant and experimental calibration of the trap stiffness is usually preferable. Techniques for position measurement will be presented in section 6.1 and methods for determining the trap stiffness are presented in section 6.2.

6.1   Position Measurements

6.1.1   Back Focal Plane Interferometry

For single trap OFM, the most accurate method for detecting the position of a trapped object is back focal plane interferometry (BFPI). An optical position sensor, such as a quadrant photo diode or position sensitive device, is positioned in a plane conjugate to the BFP of the microscope objective. When the trapped object is displaced from its equilibrium position, it changes the angle of the transmitted beam and hence its position in the BFP, which is detected by the position sensor. Position measurements with angstrom resolution have been reported [7], which, along with high temporal bandwidth suggests the use of

this method. Unfortunately, using BFPI with multiple traps in a HOT system is not feasible as light from all traps coincides in the BFP, which makes it impossible to distinguish in which trap the displacement takes place.

6.1.2   Bright Field Video Tracking

If a spherical probe particle is used, focusing of the bright field illumination light causes the center of the particle to appear brighter than the background. Detecting the lateral position of the particle is therefore readily accomplished using basic image analysis techniques. A common method for determining the position of a bright object in an image is by calculating its centroid. This is done by summing the intensity in each pixel multiplied with its x and y position and dividing with the sum of the intensity in all pixels,

$$\boldsymbol{C} = \left(\frac{\sum_{x,y} x I(x,y)}{\sum_{x,y} I(x,y)}, \frac{\sum_{x,y} y I(x,y)}{\sum_{x,y} I(x,y)} \right). \tag{6.1}$$

This gives the coordinates of the point around which the intensity of the image is equally distributed, which is a good estimate of the position of an object that does not change its shape during a measurement. Compared to simpler methods, e.g., finding the pixel with maximum brightness, the centroid method gives much higher accuracy; if the signal to noise ratio in the image is sufficiently high, the measurement error can be reduced reduced to less than 0.1 pixels [49].

Before calculating $\mathbf{C}$, it is necessary to remove any background signal from the images. The method used throughout this work is to acquire a *dark image*, with all light sources blocked, before a measurement is started, and to subtract this image and a constant value from every acquired image in the measurement. The subtraction of the dark image removes the dark current signal from each pixel, and the constant value is chosen so that all pixels outside the object are set to zero.

The centroid measurement works only when the object is brighter or darker than any other area in the image. If this condition cannot be fulfilled, more elaborate methods can be used to isolate the object from the background, e.g., by observing diffraction rings around the object. If the position of more than one object is to be determined, the image can be divided into smaller regions of interest (ROIs) each containing one object. The position of the m:th object is then simply calculated as

$$\boldsymbol{C}_m = \left(\frac{\sum_{x,y \in \mathrm{ROI_m}} x I(x,y)}{\sum_{x,y \in \mathrm{ROI_m}} I(x,y)}, \frac{\sum_{x,y \in \mathrm{ROI_m}} y I(x,y)}{\sum_{x,y \in \mathrm{ROI_m}} I(x,y)} \right). \tag{6.2}$$

Using small ROIs also reduces computation time for the centroid measurement, which may be crucial in real time applications. In some cases several ROIs can

be extracted by the camera before transfer to the computer. This increases the obtainable frame rate in cases where the frame rate is limited by the bandwidth of the computer interface.

Compared to BFP interferometry, bright field video tracking typically gives lower temporal bandwidth but the frame rate obtained with a high speed camera is in many cases sufficient. With bright field video tracking, the bandwidth is typically not restricted by the maximum frame rate itself but by the limited brightness of the microscope illumination. Frame rates beyond 10 kHz are feasible with a sensitive camera. Short shutter times with insufficient illumination reduce the signal to noise ratio, and give larger quantization errors since the dynamic range of the camera cannot be fully used. To allow for simultaneous position measurement and visual monitoring of the sample, our HOT setup is equipped with dual cameras, one high speed CMOS camera (EoSens CL MC1362, Mikrotron GmbH or MV-D1024E-CL, Photonfocus AG) for position measurements and one standard CCD camera (SCOR-20SO, Point Grey Research, Inc.) for monitoring.

6.1.3 Holographic Particle Tracking

An alternative to bright field video tracking, is holographic microscopy [21], which provides an extended measurement range in the z-direction. The sample is then illuminated with a collimated coherent light source. The interference pattern caused by the light diffracted by the object and undiffracted light is interpreted with Lorentz-Mie theory to obtain both the positions of the particles in three dimensions, their size and relative refractive index. With this method, brighter illumination, and thereby higher frame rates, can be used. However, the analysis is yet too time consuming for real time applications to be feasible.

6.2 Calibration Methods

6.2.1 Position Calibration

For bright field video tracking, the primary unit of the position vector $\mathbf{C}$ is camera pixels. This can be translated to physical position with knowledge of the pixel pitch and magnification of the microscope. Alternatively, the system can be calibrated by measuring the position of an object rigidly attached to the microscope stage while scanned across the image. Using a piezo actuated microscope stage, the latter method usually gives the highest precision. The same method may also be used for BFP interferometry and holographic particle tracking.

6.3   Force Calibration

To calculate optical forces from position measurement data, the trap stiffness, κ, must be found. Two different methods are commonly used for determining κ, drag force measurements and power spectrum measurements.

6.3.1   Drag Force Calibration

A direct way of relating the applied optical force to the response of the detection system is to apply a known force to the trapped object and read out the response from the position detector after a new equilibrium position has been found. This is conveniently done by moving the surrounding liquid relative to the particle by translating the microscope stage to create a viscous drag force. The viscous drag force, F_d on a spherical bead is described by Stokes' law, $F_d = 6\pi a\gamma v$, where a is the radius of the bead, γ is the fluid viscosity and v is the speed of the surrounding fluid relative to the bead, i.e., the speed of the microscope stage in this case since the bead is held stationary in the trap. The parameter $\gamma_0 = 6\pi a\gamma$ is called Stokes' drag coefficient and must hence be known in order to calibrate κ.

6.3.2   Power Spectrum Calibration

An alternative method for obtaining the trap stiffness is by relating the frequency spectrum of the measured Brownian motion of the trapped particle to a theoretical model. The trajectory of a trapped object can be described as an *overdamped* thermally excited harmonic oscillator. In the overdamped limit, inertial terms may be omitted and the *Langevin equation* for the motion of the particle (here in one dimension for convenience) may be written as $\gamma_0\dot{x}(t) + \kappa x(t) = \sqrt{2k_BT\gamma_0}\eta(t)$, where x is the position of the particle and $\sqrt{2k_BT\gamma_0}\eta(t)$ is a stochastic force related to the Brownian motion of the particle. Solving the Langevin equation for x in Fourier space and taking the square gives the theoretical power spectrum, which has the form of a Lorentzian function. To calibrate the trap, the position of the trapped particle is measured with high sampling frequency. The power spectrum of the position data is then fitted to the theoretical spectrum given by the Langevin equation to find κ. The theory and experimental considerations for calibration using power spectra are comprehensively reviewed in [51, 51]. The power spectrum calibration method was used to determine the uniformity of trap intensities in Paper VII.

The power spectrum and drag force methods can be combined in one measurement. This is done by applying an oscillation with known amplitude and frequency to the surrounding medium, using a piezo actuated microscope stage,

while acquiring data for the power spectrum measurement [52]. The oscillation results in a distinct peak in the power spectrum, which can be used as a reference when determining the trap stiffness. This method does not require knowledge of Stokes' drag coefficient nor a calibrated detection system. The method can also be used to probe the viscoelastic properties of non-Newtonian fluids [53, 54].

The power spectrum method requires a well aligned optical system for accurate calculation of the trap stiffness, and aberrations must be minimized since the used Langevin equation requires perfectly harmonic trapping potentials. Aberrations originating from non-flatness of the backplane of the used SLM and from other optical components in the system, can be compensated for by adding a correction matrix to generated holograms [55, 56]. Aberrations resulting from spatial variations in the phase response of the SLM are compensated for using the method described in section 5.2.2 and Paper VII.

Chapter 7

Fast Hologram Generation

7.1   Software for Hologram Generation

M any applications of HOT require a short *response time* of the system, e.g., applications including real time manipulation of traps or fast force- or position clamps. The total response time T_{tot}, here defined as the time elapsed from the input of desired spot coordinates to the hologram generating software until the SLM has physically completed the update, can be decomposed as

$$T_{tot} = T_{HG} + T_{tran} + T_{SLM}, \tag{7.1}$$

where T_{HG} is the time required for the numerical hologram generation, T_{tran} is the time required for transferring the hologram data from the computer to the SLM, and T_{SLM} is the response time of the SLM. SLMs are now available with response times down to a few milliseconds, and the time required for transferring the hologram to the SLM over a PCI-express interface is well below 1 ms. In contrast, T_{HG} for generating an optimized hologram with 512×512 pixels in Matlab is in the order of one to several seconds. This has limited the use of optimized holograms for time-critical applications. The modifications to the GS algorithm presented in Paper I, V and VI, and the high order polynomial evaluation used in the method presented in Paper VII, all further add to the computational complexity of the hologram generation and thus increase T_{HG}.

An important part of this work was to reduce the required computation time for hologram optimization including our modifications, to increase their usability also in time critical applications. Each of the methods described in Paper I, V, VI and VII was therefore implemented in the general purpose graphics processing unit (GPGPU) programming language *CUDA for C*. In recent years, GPGPU programming has been utilized in various fields of optics, enabling decreased calculation times by several orders of magnitude [57,58]. It has also been specifically demonstrated that execution on graphics processing units (GPUs) is beneficial for rapid optimization of phase-only holograms of the type

used in HOT [59, 60]. The numerical propagation steps in the GS algorithm, which constitute its most time consuming operations, are highly parallelizable and therefore well suited for execution on GPUs. When using the expressions for Fresnel summation shown in section 3.1.4 for the numerical propagation, elements of the field can be summed pairwise in a tree structure. This method is called *parallel reduction* and reduces the number of sequential operations from $N - 1$ to $logN$, where N is the number of pixels representing the field. For propagation with FFTs, a highly optimized implementation is included in the CUDA toolkit, allowing the 2D Fourier transformation of a field with $N = 512^2$ in less than 200 μs on our GPU (GeForce GTX 580, NVIDIA Corporation).

Parallel sum reductions and other matrix operations used in the algorithm have very low arithmetic intensity and are thus said to be bandwidth limited. This means that the time required for the actual computation is much shorter than the transfer time between cache memory and the global GPU memory. Additional operations, e.g., applying a lookup table in the form of a high order polynomial, as described in section 5.2.2, can therefore be done without sacrificing significantly in total response time. Implementations of GS algorithms using Fresnel summations or FFTs for numerical propagation, and including the different correction methods for LC-SLMs, are compared with regard to the required computation times in Paper III. A summary of the results is given in the following section, along with recent measurements where the hologram optimization used the method with dummy areas.

7.2 Computation Times for Hologram Generation

The hologram generating algorithms implemented in CUDA for this work includes two basic GS algorithms with weighting according to equation 3.14, one using Fresnel summations (GS-Fresnel) and one using FFTs (GS-FFT) for numerical propagation. The methods presented in sections 5.2.2 (SPVC) and 5.2.3 (RPC) were implemented for both versions of the GS algorithm. The methods presented in sections 3.6 (Dummy areas) and 5.2.1 (Crosstalk) were implemented as separate versions of the GS algorithm, using Fresnel propagation and FFTs respectively. All implementations were compiled to *dynamic-link libraries* (DLLs) which can be called from the user interface of a Labview program.

The computation times were measured for generating holograms with 3–100 desired spot positions and $N = 512^2$. For each method and number of desired spots, 250 holograms was generated and the average computation time calculated. The stated computation times include calling the DLL from Labview,
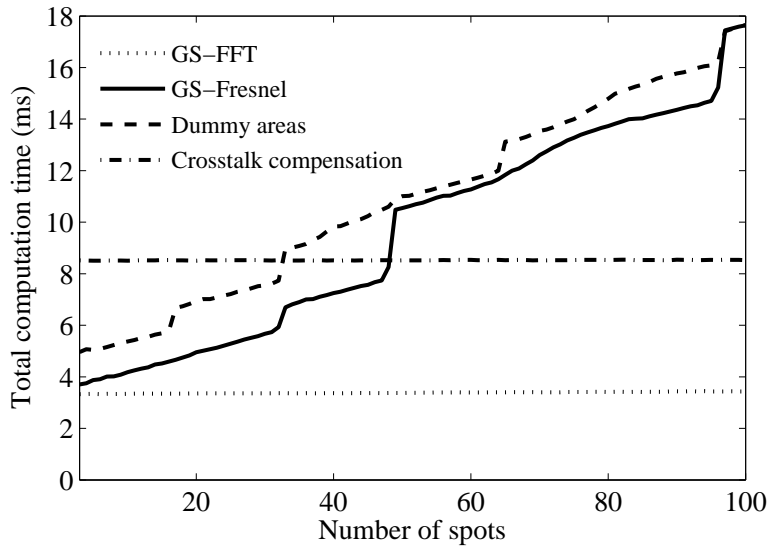
Figure 7.1: Measured computation times for generating holograms with different number of spots. Computation times given for four implementations of the GS algorithm, one using FFTs and one using Fresnel summation for numerical propagation (GS-FFT and GS-Fresnel respectively), one including crosstalk compensation and one using dummy areas for improved control of the spot intensities.

transferring the spot coordinates and desired intensities to the GPU, generating the hologram, and transferring the hologram back to the memory of the host computer.

SPVC and RPC add a constant value to the computation time, independent of the number of traps. The measured increase was 0.13 ms for the SPVC method using a seventh order polynomial, and 0.01 ms for RPC. The measured computation times for the unmodified GS algorithms and for the dummy area and crosstalk compensation methods are shown in figure 7.1. The time required for algorithms using FFTs for the numerical propagation is almost independent of the number of traps, since the entire field in the trapping plane is calculated regardless of the number of traps. Only the weight function increases the computation time slightly with the number of traps. The computation time for GS-FFT was thus found to increase very little, from 3.33 ms for 3 traps to 3.44 ms for 100 traps. My implantation of the crosstalk compensation method also uses FFTs for numerical propagation. However, the convolution step introduced for this method adds an extra pair of FFTs. Along with the extra matrix multiplication required to complete the convolution, this more than doubles the required computation time compared to the unmodified method, to 8.48 ms for 3 traps and 8.54 ms for 100 traps.

For the algorithms using Fresnel summations for numerical propagation, the computation time is strongly related to the number of spots. It does not increase linearly with the number of spots, but have discontinuities at some multiples of 16 for the GTX 580, as seen in figure 7.1. This is caused by less than optimal utilization of the 16 *multiprocessors* in our GPU for spot numbers having a small non-zero remainder for modulo 16. Other implementations eliminating this behavior were tested but were found to be slower in all cases.

From the timing measurements reported here, and in more detail in Paper III, it is obvious that of the two implementations of the unmodified GS algorithm, the FFT-based version generates holograms faster in all cases, especially for larger number of spots. However, its restrictions on the spot positioning, discussed in section 3.4, are in many cases so significant that the GS-Fresnel is preferred. The use of dummy areas adds to the computation time for implementations based on GS-Fresnel, but the increased control of trap intensities motivates its use in most situations. This implementation is now routinely used for OFM experiments in our lab. For implementations based on GS-FFT, the use of dummy areas cause no measurable increase in computation time. The increase caused by SPVC and RPC are in the order of 0–3% of T_{HG}, and can in most cases be considered negligible.

Chapter 8

Optical Trapping in LC Materials

This chapter describes a novel application of HOT, where semiconductor nanowires were trapped in LC materials and used to probe its orientational structure. The method is also described in Papers II and IV.

8.1   Nanowires in LC

As described in chapter 4, the director field is determined both by inherent properties of the LC material, and by its interaction with other materials at contact surfaces. Deformations of the director field resulting from such interactions induce elastic forces acting on the surfaces. Elongated particles suspended in an LC material are therefore spontaneously reorientated so that the elastic energy is minimized. An elongated particle causing parallel alignment of to its surfaces, suspended in a nematic LC cell, aligns with its long axis along the director of the material. Its position is not constrained but since the elastic forces increases close to the surfaces of the cell, it is pushed away from the surfaces and tend to localize near the center of the cell. Also in chiral LC will a nanowire align along the director to minimize the elastic energy. It can move with only viscous resistance in all directions but translation along the helical axis must be accompanied by a rotation following the director orientation.

8.2   Optical Trapping of Nanowires in LC

In Papers II and IV, methods for optical manipulation of nanowires in nematic and chiral nematic LC are investigated and a novel method for probing material properties is proposed.

The gallium nitride (GaN) nanowires used in these projects have very high refractive index. The large difference in refractive index to the surrounding LC material therefore prevents stable optical trapping in three dimensions, as

described in chapter 2. Placing a single optical trap near one end of a nanowire suspended in nematic LC attracts the nanowire in the lateral direction, but causes a tilt away from the trap once the nanowire reaches the trap. After removing the trap, the nanowire again aligns parallel to the substrates to minimize the elastic energy.

In chiral nematic LC, however, strong elastic forces prevents tilting of the nanowire out of the director field. The repulsive force from a laser beam instead forces the nanowire to *rotate* along with the director as it is pushed through the material. It was found that stable three dimensional trapping of the nanowire could be achieved using two traps placed at each of its ends. The nanowire could then be translated laterally by synchronous movement of the two traps, and axially by forcing a rotation of the nanowire using the traps. Since the orientation of a nanowire follows the local director, it could be used to map the structure of the material. This technique was used to study several properties of CLC materials, as described in Paper II and IV, and briefly in the following sections.

8.2.1   Local Pitch Measurements

If the separation between the substrates constituting the cell does not correspond to a half integer multiple of the natural pitch of the material, the pitch is slightly changed so that correct alignment is achieved at the surface boundaries, causing a twist deformation of the material. The pitch could be determined locally by measuring the translation in the axial direction required for a given rotation angle.

8.2.2   Probing Defects in Cholesteric LC

As in solid crystals, various defects can appear in the structure of an LC material. A common example is so called *edge dislocations*. In solid crystals, edge dislocations appear where additional layers are inserted in the crystal lattice. In CLC, the molecules have no positional order but a similar type of defect appear where one or several half twists are inserted in the helical structure of the director field. Different edge dislocations can appear depending on the number of inserted half twists, and on the orientation of the molecules in the plane of the dislocation.

When studying edge dislocations, they are usually induced in a controlled manner by varying the thickness of the LC cell from one side to the other. As the thickness of the cell increases, the pitch of the material is forced to increase until the elastic energy is lowered by the introduction of an additional 180 degree twist of the director. An edge dislocation then appears as the pitch is abruptly lowered. A wedge cell is illustrated in figure 8.1 (a) along with and illustration
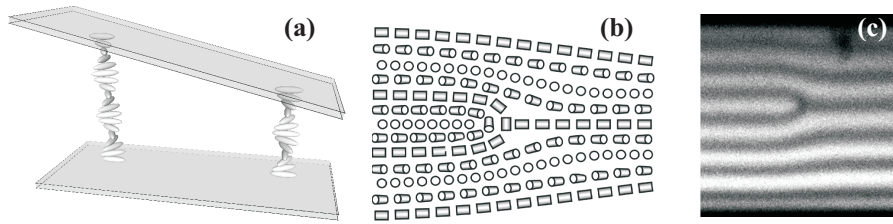
Figure 8.1: Illustration of a cholesteric LC material in a wedge cell (a) where one additional half twist of the director field in inserted on the left side so that an edge dislocation appears (b). (c) shows a confocal fluorescence polarization micrograph of the same type of edge dislocation. Figures (b) and (c) courtesy of David Engström.

of an edge dislocation (b) and a confocal fluorescence polarization micrograph (CFPM) of the same type of dislocation (c). Other types appearing in CLC are *oily streak-* and *screw dislocations*. CFPM is a method conventionally used to examine LC materials. It was used to verify our results.

By following the director field with an optically trapped nanowire, we could identify the type of the defects found in our samples. We could also study the interaction of the defects with the trapped nanowire. It was found attractive or repulsive forces could arise between defects and nanowires, depending on the type of defect and the direction of the approach. In some cases could the entire defect be pushed away by the nanowire, and in some cases was the nanowire fully enclosed by the defect line upon approach. The latter situation occurred for type of dislocation depicted in figure 8.1 (b). This dislocation has a singular point in its cross section, where the director field is undefined. Such singularity has very high elastic energy, which is lowered in the presence of the nanowire. Once enclosed by the defect, the nanowire could not be removed with the optical traps. More details on the experimental procedures and further results are presented in Paper II and IV.

Chapter 9

Conclusions

The aim of this work was to improve the beam steering accuracy in holographic optical tweezers (HOT) systems, and to explore the possibilities of using HOT for novel applications. The improvements of the beam steering method specifically aimed at reducing errors in the obtained stiffness of optical traps, previously hampering the accuracy of optical force measurements (OFM) with HOT. Four different methods for reducing stiffness errors, and a novel technique for probing the structure of liquid crystal materials using HOT were presented.

9.1   Improvements for Higher Accuracy in Optical Force Measurements

Three of the hologram design methods presented here are intended to compensate for limitations in the phase modulation of LC based SLMs, commonly used in HOT. The fourth method is beneficial for all phase-only modulating SLMs regardless of their limitations.

The response time of a nematic LC SLMs is typically in the order of 1–100 ms. During this time, transient trap intensity errors can appear due to the uncontrolled intermediate states of the SLM in the transition between two holograms. This can disturb measurements and possibly lead to the escape of trapped particles. A method for reducing these errors was presented in Paper I and summarized in section 5.2.3 of this thesis. The method relies on a modification of the hologram generating algorithm that reduces the pixelwise phase difference between consecutively displayed holograms.

The effect of crosstalk between SLM pixels was investigated in Paper VI and methods for characterizing and compensating for the crosstalk were presented. The method, summarized in section 5.2.1, relies on another modification of the hologram generating algorithm. Experimental results showed improved control

of the trap intensities and, in some cases, a reduction of unwanted light in the zeroth order diffraction spot.

Another problem commonly appearing in LC-SLMs was treated in Paper VII and in section 5.2.2, where spatial variations of the obtained phase modulation over the SLM surface for given pixel values were investigated. A new method for converting the desired phase values of a hologram to correct pixel values was presented, compensating for the spatial variations. This method leads to improved control of the spot intensities and to reduction of unwanted light in the zeroth order spot. The improvements were verified by measurements of spot intensities and in optical trapping experiments.

The fourth method is not related to non-ideal phase modulation of SLMs, but to the inherent lack of amplitude modulation. This causes the appearance of *ghost orders* in the vicinity of desired traps. The ghost orders can disturb measurements and give unwanted intensity variations when rearranging traps. The method, presented in Paper IV and summarized in section 3.6, reduces the intensity of the ghost orders by directing a fraction of the available light to dummy areas. This virtually eliminates unwanted intensity variations when rearranging traps and allows for controlled variation of the trap intensities by varying the amount of light directed to the dummy areas.

The four presented methods address the main causes for trap intensity errors in many HOT systems. Following the directions given in each paper, the errors can be significantly reduced. This improves the capability for precise force measurements, e.g., using the methods presented in chapter 6.

The presented methods all increase the computational complexity of the hologram generating algorithms to varying extent. By implementing the modified algorithms on the parallel computing platform CUDA, the required computation time is reduced so that real-time generation of holograms is feasible at rates of 50-300 Hz. This was demonstrated in Paper III and in chapter 7.

9.2   Novel Applications

A new application for HOT was presented in Papers II and IV, where optically trapped nanowires were used to probe the structure of a liquid crystal material. The nanowires suspended in the LC material could be optically trapped only in the lateral plane, due to strong scattering from their surfaces. They were, however, confined in the axial direction by interaction with the helical structure of the surrounding cholesteric LC material. The nanowire could be maneuvered in three dimensions by following the orientational structure of the material, which could thereby be mapped. Several types of defects could be classified with this method and the interaction of the nanowires with line defects was studied. It was found that the nanowires self-aligned into the defect cores

in some cases, possibly enabling self-assembly of metamaterials using liquid crystals with periodic defect structures.

9.3 Outlook

In ongoing and planned experiments, our improved HOT system is used to probe the Young's modulus of the cell wall/membranes of single yeast cells with OFM. In yeast, many proteins are involved in the synthesis of the cell wall and membrane respectively, and absence of any of them, might affect the cell wall and/or membrane stability. The elasticity of a cell can therefore reveal important information about its phenotype. The probe particles are silica microspheres whose positions are measured with bright field video tracking. The method is currently limited to measuring forces in a single plane, while the forces between the cell walls and microspheres can have components in all directions. With a more advanced particle tracking system, the benefits from our improvements could be fully utilized and the accuracy of the measurements further increased. The throughput of the experiments could also be increased by automating several steps of the measurement procedure, e.g., identification of cells suitable for measurement and alignment of the probe particles against the cells. Once an accurate and efficient measurement procedure has been established, the technique should prove useful for characterizing other microscopic systems whose viscoelastic properties are of interest.

Acknowledgement

First of all, I would like to thank my supervisor Mattias Goksör for giving me the opportunity to work in this field and for always being supportive and encouraging.

I owe my deepest gratitude to my assistant supervisor David Engström, who has guided me through my work in science since the day I joined this group. Without your support, also after leaving the group, this thesis would not have been completed. I have truly enjoyed working with you over these years.

Jörgen Bengtsson has provided invaluable input during the writing of this thesis. Thanks for your encouraging comments, for patiently correcting my errors, and for making the writing process more enjoyable.

The input from my examiner Dag Hanstorp has also helped making this thesis a better one.

Many thanks to the present and past members of the Biophotonics group: Anna-Karin, I have enjoyed sharing this office with you, thank you for putting up with my mess. Carro, Amin, Dory, Ricardo, Emma, Kristin, Rikard, Jonas, Anna and Maria, thank you all for creating such a nice work environment. The lunches in Soliden have been truly enjoyable also thanks to Maria, Johanna, Mattias, Bea and Lars.

Halina Rubinsztein-Dunlop has been a great inspiration to me ever since my first years in science. Thank you for introducing me to the field of optical trapping.

I would also like to thank Anna Linnenberger at Boulder Nonlinear Systems who has been involved in the software development related to this work. I have enjoyed working with you and hope that our collaboration will continue to bear fruit in future applications.

To my friends and family, if you have made it this far through my thesis, I wish to express my admiration. Boel, Gerda, mamma och pappa, and my fantastic friends in Stockholm and Gothenburg, thank you all for your support and encouragement throughout these years.

<div align="right">

Gothenburg, April 23, 2013
Martin Persson

</div>

References

[1] A. ASHKIN, Acceleration and Trapping of Particles by Radiation Pressure, *Physical Review Letters* **24**, 156 (1970).

[2] A. ASHKIN, Applications of laser-radiation pressure, *Science* **210**, 1081–1088 (1980).

[3] A. ASHKIN, Trapping of atoms by resonance radiation pressure, *Physical Review Letters* **40**, 729–732 (1978).

[4] A. ASHKIN, J. M. DZIEDZIC, J. E. BJORKHOLM, AND S. CHU, Observation of a single-beam gradient force optical trap for dielectric particles, *Optics Letters* **11**, 288–290 (1986).

[5] S. CHU, J. E. BJORKHOLM, A. ASHKIN, AND A. CABLE, Experiments observation of optically trapped atoms, *Physical Review Letters* **57**, 314–317 (1986).

[6] A. ASHKIN, J. M. DZIEDZIC, AND T. YAMANE, Optical trapping and manipulation of single cells using infrared laser beams, *Nature* **330**, 769–771 (1987).

[7] E. A. ABBONDANZIERI, W. J. GREENLEAF, J. W. SHAEVITZ, R. LANDICK, AND S. M. BLOCK, Direct observation of base-pair stepping by RNA polymerase, *Nature* **438**, 460–465 (2005).

[8] K. SVOBODA AND S. M. BLOCK, Force and velocity measured for single kinesin molecules, *Cell* **77**, 773–784 (1994).

[9] E. R. DUFRESNE, G. C. SPALDING, M. T. DEARING, S. A. SHEETS, AND D. G. GRIER, Computer-generated holographic optical tweezer arrays, *Review of Scientific Instruments* **72**, 1810–1816 (2001).

[10] M. REICHERTER, T. HAIST, E. U. WAGEMANN, AND H. J. TIZIANI, Optical particle trapping with computer-generated holograms written on a liquid-crystal display, *Optics Letters* **24**, 608–610 (1999).

[11] A. van der Horst and N. R. Forde, Calibration of dynamic holographic optical tweezers for force measurements on biomaterials, *Optics Express* **16**, 20987–21003 (2008).

[12] C. O. Mejean, A. W. Schaefer, E. A. Millman, P. Forscher, and E. R. Dufresne, Multiplexed force measurements on live cells with holographic optical tweezers, *Optics Express* **17**, 6209–6217 (2009).

[13] A. Farré, A. van der Horst, G. A. Blab, B. P. B. Downing, and N. R. Forde, Stretching single DNA molecules to demonstrate high-force capabilities of holographic optical tweezers, *Journal of Biophotonics* **3**, 224–233 (2010).

[14] D. Preece, R. Bowman, A. Linnenberger, G. Gibson, S. Serati, and M. Padgett, Increasing trap stiffness with position clamping in holographic optical tweezers, *Optics Express* **17**, 22718–22725 (2009).

[15] M. Reicherter, S. Zwick, T. Haist, C. Kohler, H. Tiziani, and W. Osten, Fast digital hologram generation and adaptive force measurement in liquid-crystal-display-based holographic tweezers, *Appl. Opt.* **45**, 888–896 (2006).

[16] P. Lebedev, Untersuchungen über die Druckkräfte des Lichtes, *Annalen der Physik* **311**, 433–458 (1901).

[17] Y. Harada and T. Asakura, Radiation forces on a dielectric sphere in the Rayleigh scattering regime, *Optics Communications* **124**, 529–541 (1996).

[18] T. A. Nieminen, H. Rubinsztein-Dunlop, and N. R. Heckenberg, Calculation of the T-matrix: general considerations and application of the point-matching method, *Journal of Quantitative Spectroscopy and Radiative Transfer* **79-80**, 1019–1029 (2003).

[19] K. C. Neuman, E. H. Chadd, G. F. Liou, K. Bergman, and S. M. Block, Characterization of photodamage to Escherichia coli in optical traps, *Biophysical Journal* **77**, 2856–2863 (1999).

[20] H. Liang, K. T. Vu, P. Krishnan, T. C. Trang, D. Shin, S. Kimel, and M. W. Berns, Wavelength dependence of cell cloning efficiency after optical trapping, *Biophysical Journal* **70**, 1529–1533 (1996).

[21] W. M. Lee, P. J. Reece, R. F. Marchington, N. K. Metzger, and K. Dholakia, Construction and calibration of an optical trap on a fluorescence optical microscope, *Nature Protocols* **2**, 3226–3238 (2007).

[22] E. FÄLLMAN AND O. AXNER, Design for fully steerable dual-trap optical tweezers, *Applied Optics* **36**, 2107–2113 (1997).

[23] K. VISSCHER, G. J. BRAKENHOFF, AND J. J. KROL, Micromanipulation by "multiple" optical traps created by a single fast scanning trap integrated with the bilateral confocal scanning laser microscope, *Cytometry* **14**, 105–114 (1993).

[24] J. W. GOODMAN, *Introduction To Fourier Optics*, McGraw-Hill, 2 edition (1996).

[25] L. B. LESEM, P. M. HIRSCH, AND J. A. JORDAN, Kinoform - a new wavefront reconstruction device, *Ibm Journal of Research and Development* **13**, 150–155 (1969).

[26] N. C. GALLAGHER AND B. LIU, Method for computing kinoforms that reduces image reconstruction error, *Appl. Opt.* **12**, 2328–2335 (1973).

[27] A. GEORGIOU, Noise formation in Fourier phase-only holograms, *J. Opt. Soc. Am. B* **27**, 2677–2686 (2010).

[28] J. E. CURTIS, C. H. J. SCHMITZ, AND J. P. SPATZ, Symmetry dependence of holograms for optical trapping, *Optics Letters* **30**, 2086–2088 (2005).

[29] W. O. GERCHBERG, R. W.; SAXTON, Practical algorithm for determination of phase from image and diffraction plane pictures, *Optik* **35**, 237–246 (1972).

[30] P. M. HIRSCH, J. A. JORDAN JR., AND L. B. LESEM. Method of making an object dependent diffuser (1971).

[31] J. R. FIENUP, Reconstruction of an object from modulus of its fourier-transform, *Optics Letters* **3**, 27–29 (1978).

[32] V. V. KOTLYAR, P. G. SERAPHIMOVICH, AND V. A. SOIFER, An iterative weight-based method for calculating kinoforms, In N. A. Kuznetsov and V. A. Soifer, editors, *5th International Workshop on Image Processing and Computer Optics*, volume 2363 of *Proc. SPIE*, pages 177–183 (1995).

[33] J. R. FIENUP, Phase retrieval algorithms - a comparison, *Applied Optics* **21**, 2758–2769 (1982).

[34] J. E. CURTIS, B. A. KOSS, AND D. G. GRIER, Dynamic holographic optical tweezers, *Optics Communications* **207**, 169–175 (2002).

[35] R. Di Leonardo, F. Ianni, and G. Ruocco, Computer generation of optimal holograms for optical trap arrays, *Optics Express* **15**, 1913–1922 (2007).

[36] M. W. Farn, *New iterative algorithm for the design of phase-only gratings*, volume 1555 of *Proceedings of the Society of Photo-Optical Instrumentation Engineers (Spie)*, pages 34–42, Spie - Int Soc Optical Engineering, Bellingham (1991).

[37] J. Bengtsson, Kinoform design with an optimal-rotation-angle method, *Appl. Opt.* **33**, 6879–6884 (1994).

[38] H. Akahori, Spectrum leveling by an iterative algorithm with a dummy area for synthesizing the kinoform, *Appl. Opt.* **25**, 802–811 Mar 1986.

[39] A. Georgiou, J. Christmas, N. Collings, J. Moore, and W. A. Crossland, Aspects of hologram calculation for video frames, *Journal of Optics A: Pure and Applied Optics* **10**, 035302 (2008).

[40] P. De Gennes, *The Physics of Liquid Crystals*, International Series of Monographs on Physics, Clarendon Press (1974).

[41] E. Hällstig, J. Stigwall, T. Martin, L. Sjöqvist, and M. Lindgren, Fringing fields in a liquid crystal spatial light modulator for beam steering, *Journal of Modern Optics* **51**, 1233–1247 (2004).

[42] T. H. Barnes, K. Matsumoto, T. Eiju, K. Matsuda, and N. Ooyama, Grating interferometer with extremely high stability, suitable for measuring small refractive index changes, *Appl. Opt.* **30**, 745–751 (1991).

[43] J. L. McClain, P. S. Erbach, D. A. Gregory, and F. T. S. Yu, Spatial light modulator phase depth determination from optical diffraction information, *Optical Engineering* **35**, 951–954 (1996).

[44] D. Engström, G. Milewski, J. Bengtsson, and S. Galt, Diffraction-based determination of the phase modulation for general spatial light modulators, *Applied Optics* **45**, 7195–7204 (2006).

[45] J. W. Tay, M. A. Taylor, and W. P. Bowen, Sagnac-interferometer-based characterization of spatial light modulators, *Appl. Opt.* **48**, 2236–2242 (2009).

[46] J. Otón, P. Ambs, M. S. Millán, and E. Pérez-Cabré, Multipoint phase calibration for improved compensation of inherent wavefront distortion in parallel aligned liquid crystal on silicon displays, *Appl. Opt.* **46**, 5667–5679 Aug 2007.

[47] X. Xun and R. W. Cohn, Phase calibration of spatially nonuniform spatial light modulators, *Appl. Opt.* **43**, 6400–6406 (2004).

[48] G. Thalhammer, R. W. Bowman, G. D. Love, M. J. Padgett, and M. Ritsch-Marte, Speeding up liquid crystal SLMs using overdrive with phase change reduction, *Opt. Express* **21**, 1779–1797 Jan 2013.

[49] J. C. Crocker and D. G. Grier, Methods of Digital Video Microscopy for Colloidal Studies, *Journal of Colloid and Interface Science* **179**, 298–310 (1996).

[50] T. A. Nieminen and et al., Optical tweezers computational toolbox, *Journal of Optics A: Pure and Applied Optics* **9**, S196 (2007).

[51] K. Berg-Sørensen and H. Flyvbjerg, Power spectrum analysis for optical tweezers, *Review of Scientific Instruments* **75**, 594–612 (2004).

[52] S. F. Tolic-Norrelykke, E. Schaffer, J. Howard, F. S. Pavone, F. Julicher, and H. Flyvbjerg, Calibration of optical tweezers with positional detection in the back focal plane, *Review of Scientific Instruments* **77**, 103101–11 (2006).

[53] S. H. Roelofs, M. B. Alvarez-Elizondo, T. A. Nieminen, M. Persson, N. Heckenberg, and H. Rubinsztein-Dunlop, *Calibration of trap stiffness and viscoelasticity in polymer solutions - art. no. 703823*, volume 7038 of *Proceedings of the Society of Photo-Optical Instrumentation Engineers (Spie)*, pages 3823–3823, Spie-Int Soc Optical Engineering, Bellingham (2008).

[54] F. Mario and B.-S. Kirstine, Calibration of trapping force and response function of optical tweezers in viscoelastic media, *Journal of Optics A: Pure and Applied Optics* **9**, S239 (2007).

[55] A. Jesacher, A. Schwaighofer, S. Fürhapter, C. Maurer, S. Bernet, and M. Ritsch-Marte, Wavefront correction of spatial light modulators using an optical vortex image, *Opt. Express* **15**, 5801–5808 Apr 2007.

[56] T. Cizmar, M. Mazilu, and K. Dholakia, In situ wavefront correction and its application to micromanipulation, *Nat Photon* **4**, 388–394 (2010).

[57] E. Alerstam, T. Svensson, and S. Andersson-Engels, Parallel computing with graphics processing units for high-speed Monte Carlo simulation of photon migration, *Journal of Biomedical Optics* **13** (2008).

[58] T. Shimobaba, Y. Sato, J. Miura, M. Takenouchi, and T. Ito, Real-time digital holographic microscopy using the graphic processing unit, *Optics Express* **16**, 11776–11781 (2008).

[59] A. Hermerschmidt, S. Kruger, T. Haist, S. Zwick, M. Warber, and W. Osten, *Holographic optical tweezers with real-time hologram calculation using a phase-only modulating LCOS-based SLM at 1064 nm - art. no. 690508*, volume 6905 of *Proceedings of the Society of Photo-Optical Instrumentation Engineers (Spie)*, pages 90508–90508, Spie-Int Soc Optical Engineering, Bellingham (2008).

[60] S. Bianchi and R. Di Leonardo, Real-time optical micro-manipulation using optimized holograms generated on the GPU, *Computer Physics Communications* **181**, 1442–1446 (2010).